



Instrumentation and Aerothermal Postflight Analysis of the Rocket Technology Flight Experiment ROTEX-T

T. Thiele* and A. Gülnan†

DLR, German Aerospace Center, 51147 Cologne, Germany

and

H. Olivier‡

RWTH Aachen University, 52056 Aachen, Germany

DOI: 10.2514/1.A34129

Based on experience gathered during the Sharp Edge Hypersonic Flight Experiments SHEFEX-I and SHEFEX-II the German Aerospace Center performed the Rocket Technology Flight Experiment-Transition (ROTEX-T). ROTEX-T was successfully launched on 19 July 2016 from the Esrange Space Center near Kiruna in northern Sweden. ROTEX-T was a low-cost flight experiment mission without an inertial measurement unit, reaction control system, or parachute. The payload reached an altitude of 183 km, performed a ballistic reentry with a total flight time of approximately 446 s, and was afterward recovered by helicopter. A unique and modular data acquisition system with sampling rates of 20 Hz, 1 kHz, 10 kHz, and 2000 kHz was developed for ROTEX-T to study also instationary aerothermal phenomena. All flight data were transmitted via telemetry during flight or downloaded from the onboard memory units after recovery. Using the measured surface pressures and two different analytical/numerical methods, the vehicle attitude was calculated for ascent and reentry. The computations gave adequate results for the angle of attack and sideslip within the accuracy of the described methods. The measurements of the heat flux microsensors were compared with calculated values of two analytical and one numerical approaches. An overall reasonable agreement was achieved between computations and measurements for laminar and turbulent levels with deviations between 15.4 and 19.5% at maximum heating. In addition to the heat flux sensors, the heat flux was also derived from temperature measurements of coaxial thermocouples. For the first 33 s of the ascent phase, the derived heat fluxes agreed well with measurements of the heat flux microsensors to within 0.8–5% at maximum heating levels. After that instant of time, the heat fluxes start to differ significantly due to violation of the semi-infinite wall assumption and thermocouple heating by transversal conduction.

Nomenclature

c	=	specific heat capacity, $\text{J} \cdot \text{kg}^{-1} \cdot \text{K}^{-1}$
c_f	=	local skin-friction coefficient
c_p	=	pressure coefficient
F	=	temperature ratio (wall to boundary-layer edge)
F_c, F_x	=	transfer functions for local skin-friction coefficient
F_θ	=	dynamic viscosity ratio (boundary-layer edge to wall)
h	=	height, km
K	=	mixing length proportionality factor
k	=	thermal conductivity, $\text{W} \cdot \text{m}^{-1} \cdot \text{K}^{-1}$
M	=	Mach number
n	=	unit normal vector
Pr	=	Prandtl number
p	=	pressure, Pa
\dot{q}	=	heat flux rate, $\text{W} \cdot \text{m}^{-2}$
Re	=	Reynolds number
Re_{af}	=	Reynolds analogy factor
r	=	recovery factor (equal to $(T_r - T_e)/(T_0 - T_e)$)
St	=	Stanton number
T	=	temperature, K
T_e	=	boundary-layer edge temperature, K

T_r	=	recovery temperature, K
T_0	=	total temperature, K
T^*	=	reference temperature (reference method), K
t	=	time, s
u, v, w	=	components of velocity vector, $\text{m} \cdot \text{s}^{-1}$
V	=	velocity vector
x, y, z	=	coordinates, m
α	=	angle of attack, deg
β	=	angle of sideslip, deg
γ	=	heat capacity ratio
δ	=	cone angle, deg
θ	=	local deflection angle, deg
μ	=	dynamic viscosity, $\text{Pa} \cdot \text{s}$
ρ	=	density, $\text{kg} \cdot \text{m}^{-3}$

Subscripts

calc	=	calculated
CFD	=	computational fluid dynamics
e	=	boundary-layer edge condition
i	=	index
lam	=	laminar
max	=	maximum
meas	=	measured
n	=	index
TM	=	Taylor–MacColl
tur	=	turbulent
w	=	wall condition
∞	=	inflow condition

Presented as Paper 2017-2208 at the 21st AIAA International Space Planes and Hypersonics Technologies Conference, Xiamen, China, 6–9 March 2017; received 27 October 2017; revision received 31 January 2018; accepted for publication 26 March 2018; published online 28 June 2018. Copyright © 2018 by German Aerospace Center. Published by the American Institute of Aeronautics and Astronautics, Inc., with permission. All requests for copying and permission to reprint should be submitted to CCC at www.copyright.com; employ the ISSN 0022-4650 (print) or 1533-6794 (online) to initiate your request. See also AIAA Rights and Permissions www.aiaa.org/randp.

*Research Scientist, Supersonic and Hypersonic Technologies Department, Institute of Aerodynamics and Flow Technology.

†Head, Supersonic and Hypersonic Technologies Department, Institute of Aerodynamics and Flow Technology.

‡Head, Shock Wave Laboratory.

I. Introduction

LOW-COST access to space requires efficient and reliable design tools to reduce the design margins to a minimum. Although ground testing still provides the main design verification, a complete

simulation of the flight conditions is usually not possible. Therefore, flight experiments are the most effective tool to obtain validation data under real flight conditions. The flight data can then be used to validate and improve analysis and design tools for future missions.

As the flight environment is complex and the flight trajectory has almost a continuous transitional character, the corresponding instrumentation and data acquisition system have to be designed accordingly. The response time of the sensors has to be minimized, while the sampling rate should be as high as possible. Since parameter studies during high-speed flight experiments are extremely limited, complementary use of ground testing facilities and computational fluid dynamics (CFD) is essential.

To gain flight data in hypersonic flight regimes, the German Aerospace Center (hereafter, DLR) successfully performed the flight experiments SHEFEX-I [1] and SHEFEX-II [2–5]. Compared to SHEFEX-I, which reached Mach numbers up to 6.5, SHEFEX-II achieved a maximum Mach number of 9.3 and was equipped with a higher number of sensors including a flush air data sensing (FADS) system for the sharp-edged configuration. Based on this experience, DLR performed the flight experiment ROTEX-T, which was successfully launched on 19 July 2016 at 06:05 a.m. Central European summer time from the Esrange Space Center near Kiruna in northern Sweden.

Sections II and III of this paper describe the ROTEX-T flight configuration and its instrumentation. The flown trajectory including main flight parameters is presented in Sec. IV together with results of the measured sensor data. Finally, the main outcomes of the experiment are summarized in Sec. V.

II. Flight Configuration and Integration

The complete flight configuration with a length of 10 m on the launch pad is shown in Fig. 1. The ROTEX-T payload was launched on a two-stage unguided rocket motor configuration. The first stage consisted of the solid propellant motor Terrier Mk12, and for the second stage, an Improved Orion (military M112 Hawk) motor, also driven by solid propellant, was used. The Terrier motor had a burn phase of 5 s. The Improved Orion motor is a dual-thrust burner with a boost phase of 5 s and a sustainer phase of approximately 21 s. During the complete acceleration phase of approximately 40 s, a peak acceleration of about 19.4 g was reached.

The overall length of the payload including all service modules and motor adapter was 3.013 m with a diameter of 356 mm. This led to a total payload mass (including motor adapter and balance masses) of about 190 kg. Figure 2 shows the payload mounted to the second-stage motor on its way to the launch pad. The front part of the payload consisted of a cone with a half-angle of 7 deg and a length of 1041 mm. A conical flare with 20 deg deflection angle and a length of 132 mm was attached to the cone. To measure key aerothermal parameters during flight, these two parts, which represent the main



Fig. 1 ROTEX-T complete configuration at the launcher.



Fig. 2 ROTEX-T payload mounted to second stage.

scientific part of the payload, were instrumented with a large number of sensors. The instrumentation included absolute pressure sensors, small piezoelectric dynamic pressure sensors with very high sampling frequency, heat flux sensors, coaxial thermocouples, and structural thermocouples. Behind the conical flare, two experiment service modules with a length of 400 mm each, containing the necessary electronic boxes for data acquisition, were used. The first service module was also equipped with several heat flux and pressure sensors. Three further modules were located between the experiment service modules and the second-stage motor, which were provided by the DLR Mobile Rocket Base (MORABA) department. These modules contained further necessary electronics, which is described later on. The complete payload layout is shown in Fig. 3.

The 7 deg stainless steel cone consisted of two halves for easier instrumentation. To avoid screw connections on the outer surface, the two halves were joined together using a dovetail connection. Because of the very precise manufacturing of the dovetail connection, no steps nor gaps were visible between the two halves after assembly. The nose part of the cone was manufactured as a separate solid part because it was not possible to manufacture the dovetail connection to the very tip of the cone halves. This nose part with a length of 141 mm and a nose radius of 2.5 mm also acted as a fixation for the two cone halves. As the highest temperatures occur at the nose tip, the nose part was manufactured from high-temperature steel INCONEL 600.

The 20 deg conical flare part, which was made from stainless steel, also consisted of two halves for easier instrumentation. Because more space for mounting was available inside this part, the two halves were joined by eight M6 screws that were located internally, and no dovetail connection was necessary. But a tongue-and-groove joint was manufactured between the two halves that acted as a kind of sealing. After the instrumentation was completed, the 20 deg flare part was mounted to the 7 deg cone by 20 M8 screws.

Nearly all sensors were mounted via simple screw connections. Only the cylindrical piezoelectric dynamic pressure sensors were glued into boreholes with high-temperature silicone. To route the harness of sensors and electronic boxes, several cable guides were installed in the interior. The cable guides were located near the axis of the vehicle to prevent the cables coming in contact with the hot wall during flight; see Fig. 4.

Beside the main electronic boxes for data acquisition, located in the experiment service modules, several small front-end electronic boxes were necessary for the high-speed data acquisition systems (sampling frequencies 10 and 2000 kHz). These boxes were placed inside the cone and flare parts near the sensors for sensor signal amplification and analog-to-digital conversion. The digitized sensor signals were then sent to the main electronic box in the first experiment service module. The front-end electronic boxes can be seen in Figs. 4 and 5, in which the cone and flare halves are shown during instrumentation (e.g., the left side of Fig. 5, lower left corner). The four golden colored boxes located in the flare halves were used as breakout boxes between sensor cables and the payload harness connected to the electronic boxes in the service modules.

The two experiment service modules were manufactured from black anodized aluminum. The first service module contained the high-speed data acquisition system used for all piezoelectric dynamic pressure sensors (sampling frequency 2000 kHz) and part of the absolute pressure sensors and coaxial thermocouples (sampling frequency 10 kHz). This system, integrated into a cylindrical housing and mounted to the aluminum bulkhead, also included a crash-resistant memory, which was necessary because not all data could be

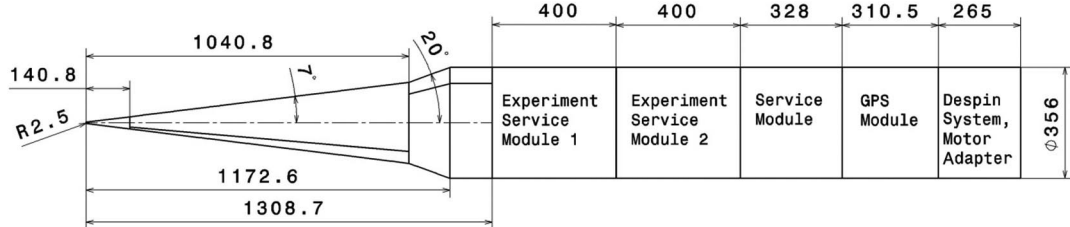


Fig. 3 ROTEX-T payload overview.

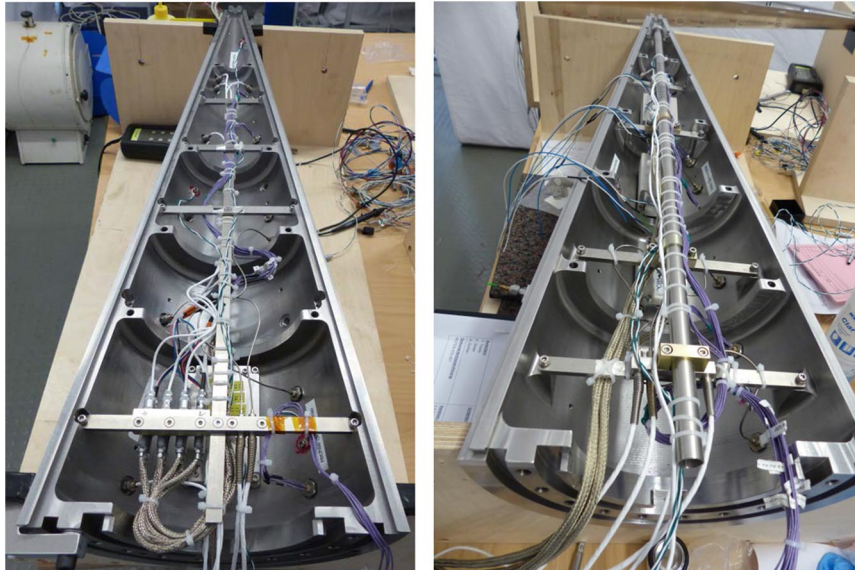


Fig. 4 ROTEX-T 7 deg cone halves during instrumentation.

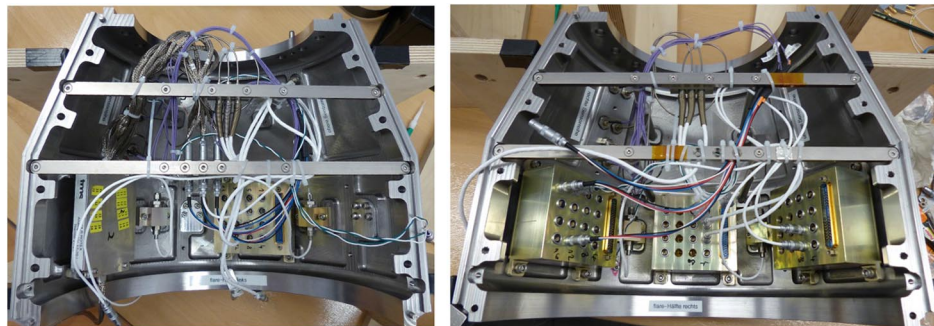


Fig. 5 ROTEX-T 20 deg flare halves during instrumentation.

transmitted to the ground station due to the high sampling frequency and limited telemetry bandwidth. The second experiment service module contained the low-speed data acquisition system (sampling frequency 20 Hz) and the medium-speed data acquisition system (sampling frequency 1 kHz), including a crash-resistant memory unit in a separate box and four high-definition (HD) cameras including their mechanical interface. The umbilical connector, used for payload testing after assembly, was also integrated into the second service module. The experiment service modules were mounted by a so-called Radial-Axial (RADAX) joint, which was also used for the connection between the flare part and first experiment service module. The joint consisted of 30 M5 screws equally spaced every 12 deg in the circumferential direction. The first and second experiment service modules during assembly are presented in Fig. 6.

In addition to the two experiment service modules, three further cylindrical modules were attached to the payload as shown in Fig. 3. These modules, provided by DLR department MORABA, contained batteries, a telemetry transmitter including an antenna, a GPS system

receiver, a wrap-around antenna for GPS, and a necessary ignition unit for vehicle time events (e.g., ignition second stage, yo-yo despin, and payload separation). The lowermost module also included the despin system and the motor adapter serving as an interface between the payload and second-stage motor. The despin system consisted of two small masses attached to a steel cable, which was wrapped around the module in a corresponding groove.

Besides the instrumentation of the payload itself, one of the second-stage fins and the tailcan of the second stage were also instrumented with thermocouples and strain gauges. The two necessary small electronic boxes were mounted to the interior of the tailcan as shown in Fig. 7.

To connect the two electronic boxes in the tailcan to the telemetry and power system in the service module, a cable was attached to the outer surface of the motor case. Two feedthroughs in the motor adapter and tailcan were used for the cable routing. To protect the cable during flight, it was covered with adhesive aluminum tape and a thick layer of red high-temperature silicone as shown in Fig. 8.

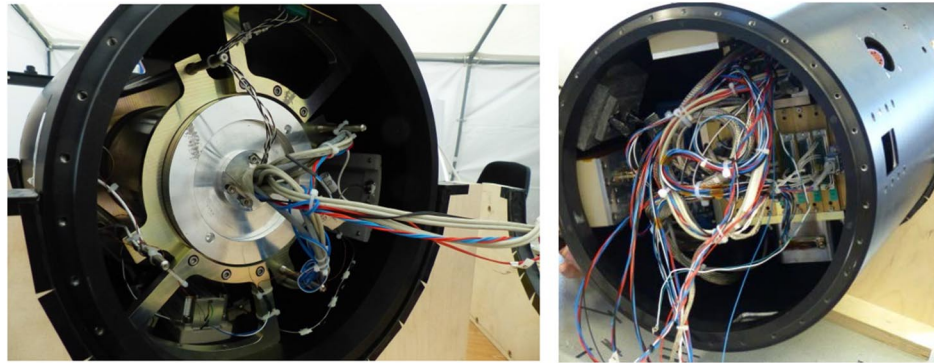


Fig. 6 First (left) and second (right) experiment service modules during integration.

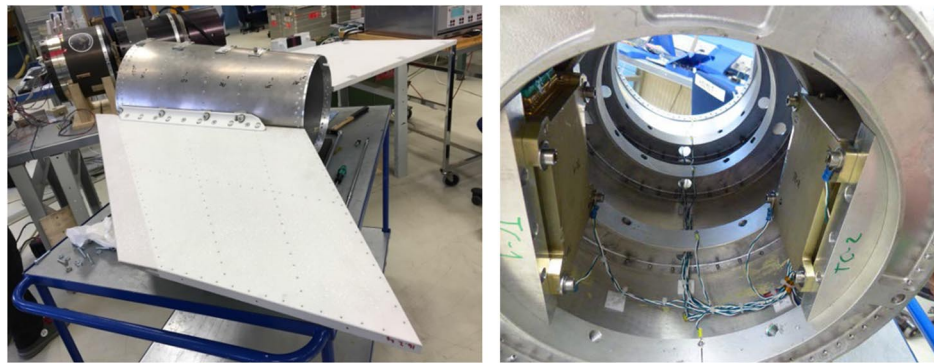


Fig. 7 Fin integration to tailcan (left) and electronic boxes mounted to tailcan interior (right).



Fig. 8 Cable routing between tailcan and motor adapter of Improved Orion second-stage.

III. Instrumentation

The ROTEX-T flight experiment was equipped with 96 sensors and four HD cameras. Table 1 presents an overview of the used sensors and locations.

For absolute surface pressure measurements, pressure transducers of the type XTE-190M of the Kulite Company were used with a

measurement range of 1.7 bar. For one pressure transducer (KU7, see Fig. 9) on the flare, a higher measurement range of 3.5 bar was used. The sensors on the cone were mounted flush with the surface, as their maximum operating temperature of 273°C was well above the expected surface temperatures. As the predicted temperatures on the flare surface exceeded the maximum operating temperature, all pressure sensors on the flare, except for transducer KU7, were mounted to aluminum blocks, which in turn were fixed using thermal spacers made of polyether ether ketone (PEEK) material with low thermal conductivity. For the connection to the flare surface, stainless steel pressure ports and metallic tubing were used. The pressure sensor fixation for the flare pressure sensors is shown in Fig. 10 (see also Fig. 5).

As the surface temperatures on experiment service module 1 were expected to remain below 200°C, the three pressure sensors on this module were integrated flush with the surface. The absolute pressure sensors on the cone and flare were sampled with different frequencies according to Figs. 9 and 11–13.

For the first time, piezoelectric dynamic pressure sensors of the PCB Piezotronics company were used during a hypersonic flight to measure the pressure fluctuations with a sampling rate of 2 MHz. The abbreviation PCB stands for picocoulomb and is also a registered trademark of the company. Because of the high-frequency sampling,

Table 1 ROTEX-T instrumentation overview

Sensor type	Nose part	Cone	Flare	Experiment service module 1	Experiment service module 2	Second-stage tailcan	Second-stage fin
Absolute pressure sensor	—	9	5	3	—	—	—
Dynamic pressure sensor	—	6	—	2	—	—	—
Heat flux microsensor	—	5	6	3	—	—	—
Coaxial thermocouple	—	10	6	—	—	—	—
Structure thermocouple	2	6	4	3	3	13	6
Full-bridge strain gauge	—	—	—	—	—	—	3
Strain-gauge rosette 0/45/90 deg	—	—	—	—	—	—	1
HD cameras	—	—	—	—	4	—	—

- | | |
|----------------------------|----------------------|
| ○ Absolute pressure sensor | Sampling rate 10 kHz |
| □ PCB pressure sensor | Sampling rate 20 Hz |
| △ Coaxial thermocouple | Sampling rate 1 kHz |
| ✗ Heat flux microsensor | Sampling rate 2 MHz |

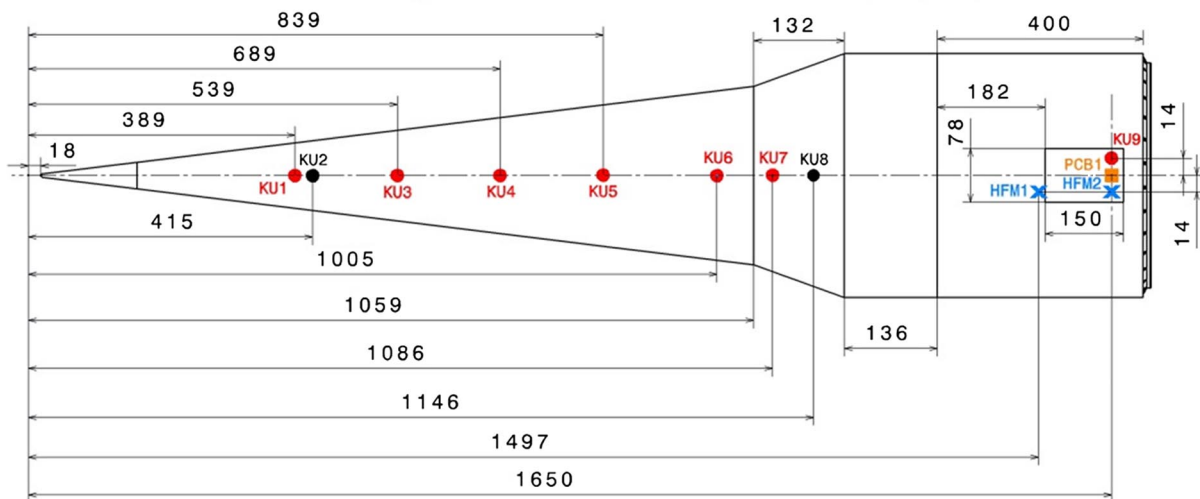


Fig. 9 ROTEX-T payload sensors top line (0 deg).

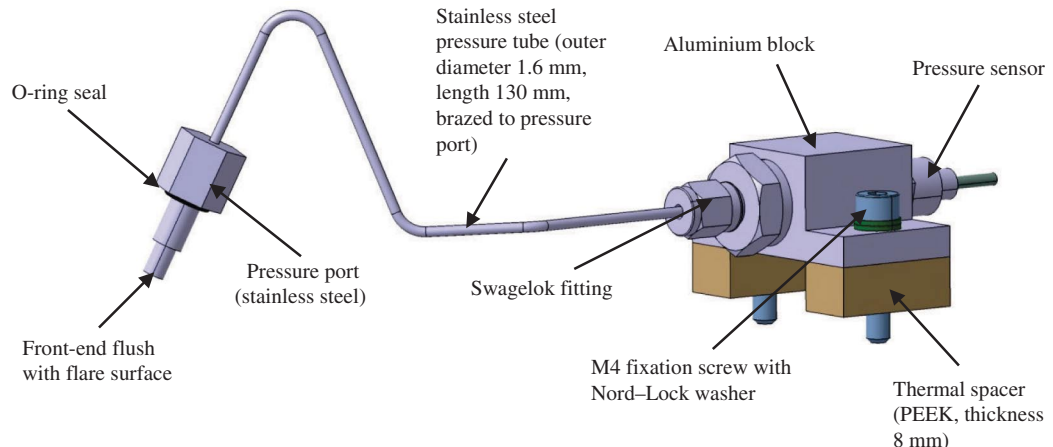


Fig. 10 Pressure sensor mounting for the flare.

- | | |
|----------------------------|----------------------|
| ○ Absolute pressure sensor | Sampling rate 10 kHz |
| □ PCB pressure sensor | Sampling rate 20 Hz |
| △ Coaxial thermocouple | Sampling rate 1 kHz |
| ✗ Heat flux microsensor | Sampling rate 2 MHz |

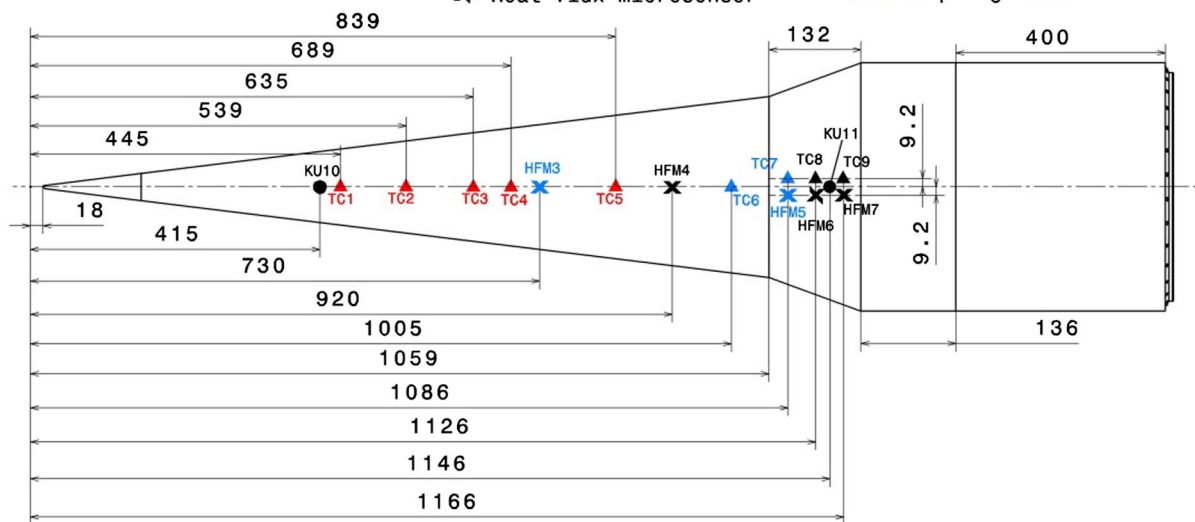


Fig. 11 ROTEX-T payload sensors right line (90 deg).

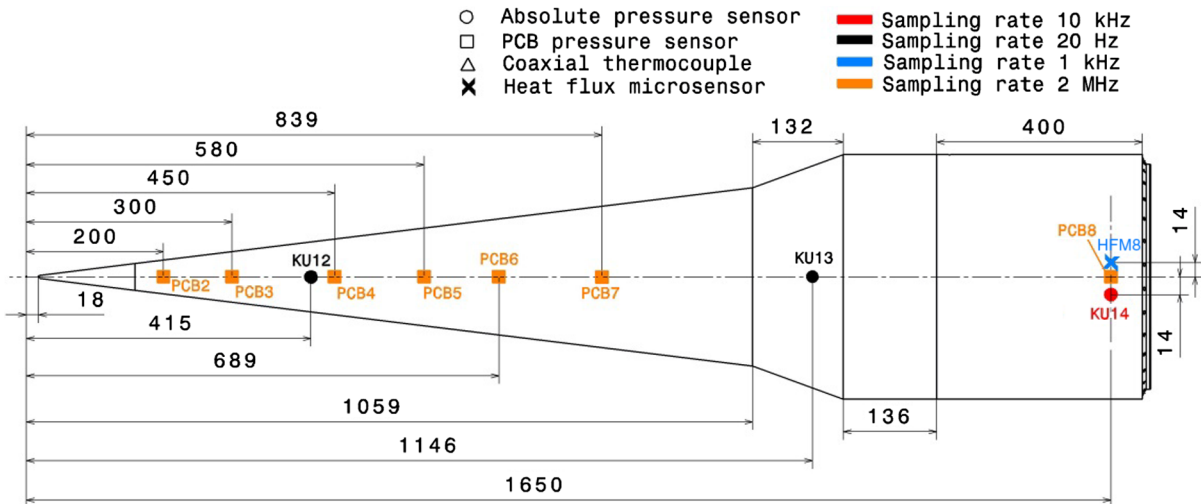


Fig. 12 ROTEX-T payload sensors bottom line (180 deg).

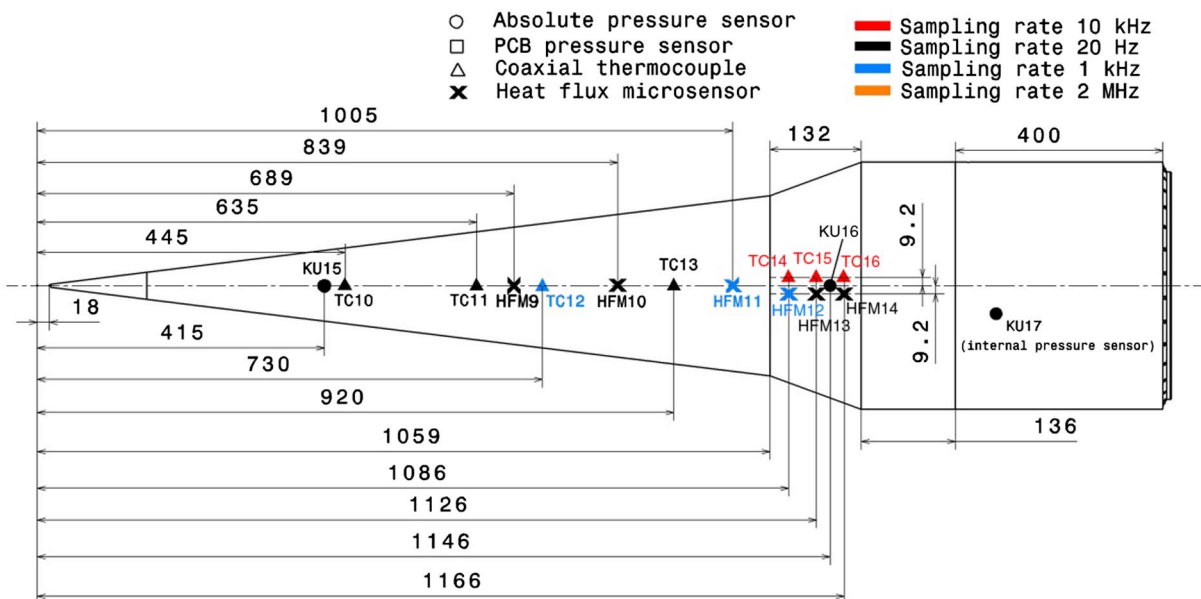


Fig. 13 ROTEX-T payload sensors left line (270 deg).

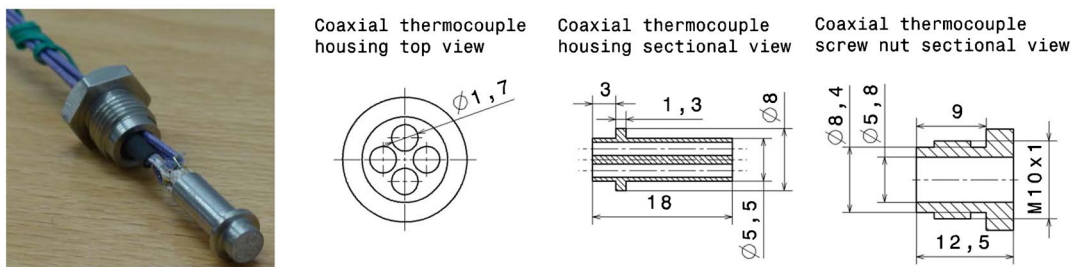


Fig. 14 Coaxial thermocouple used for the cone instrumentation.

all dynamic pressure sensors were integrated flush with the surface using high-temperature silicone glue. The data of the PCB sensors are still being analyzed, and therefore no PCB flight data were included in this paper.

Based on SHEFEX-I and SHEFEX-II heritage, total heat flux measurements were carried out using heat flux microsensors (HFM)s (type 7E/H) of the Vatell Company. These sensors have a maximum operating temperature of 400°C (600°C for short duration), which was sufficient for the ROTEX-T flight, even for the locations on the flare.

Coaxial thermocouples of the Shock Wave Laboratory of the Rheinisch Westfälische Technische Hochschule Aachen University

were used for fast surface temperature measurements [6]. For ROTEX-T, a new coaxial thermocouple version was developed and consisted of four individual coaxial thermocouples (type E) in one sensor housing connected in series to increase sensitivity. Figure 14 shows an image and a technical drawing of this thermocouple version including a screw nut for fixation. In general, measured surface temperatures can be used to calculate the surface heat flux by assuming one-dimensional heat conduction and a semi-infinite wall. But the semi-infinite wall assumption is only valid until the rear-end temperature of the sensor is increasing. Therefore, the temperature at the rear end of the sensor was also measured by a separate

thermocouple incorporated in the sensor design. The sensor design with four individual thermocouples connected in series was used for measurements on the cone. Because of the higher heat fluxes on the flare, a similar design with an identical sensor housing but incorporating only a single coaxial thermocouple was used for the flare measurements.

In addition to the temperature measurements on the vehicle surface, several standard type-K thermocouples were attached to the interior structure of the cone and flare to measure the inner temperature distribution. Further type-K thermocouples were integrated into the fin and tailcan of the second-stage motor to measure the structure temperatures. The fin was also equipped with strain gauges to measure the deformation in different axes during ascent and reentry.

Figures 9 and 11–13 show the sensor distribution on the surface of the cone, flare, and experiment service module 1. The figures also show the allocation of the sensors to the different data acquisition systems.

The instrumentation layout of the second-stage fin is presented in Fig. 15. Three full-bridge strain gauges were attached to the fin frame, and one strain-gauge rosette was fixed to the fin cover sheet. At each measurement location, a thermocouple was installed near the strain gauges. Two further thermocouples were integrated into the fin leading edge.

The tailcan was instrumented with 13 type-K thermocouples, mounted to the tailcan frames, tailcan cladding, and electronic boxes. In Fig. 16, the thermocouple positions on tailcan frames and cladding are shown. Thermocouples (TCs) TC1–TC5 were mounted to the inner surface of the tailcan cladding, and TC6–TC9 were fixed to the inner side of the tailcan frames. All tailcan thermocouples had a ring lug for fixation using screws. The thermocouples TC10–TC13 were attached to the fixation screws of the two electronic boxes mounted inside the tailcan (see Fig. 7).

Overall, three different data acquisition systems (low-speed, medium-speed, and high-speed), partially including a separate crash-resistant memory unit, and four camera modules were used for the ROTEX-T flight experiment. A detailed description of these systems is presented in a separate paper [7].

The measurement uncertainties for pressure, temperature, and heat flux sensors are summarized in Table 2. The measurement uncertainty for the heat flux microsensor is within $\pm 5\%$ to $\pm 10\%$. The manufacturer states a measurement uncertainty of $\pm 5\%$ combining repeatability and calibration accuracy. But several wind-tunnel tests for which the same sensor was used and compared with different types of heat flux gauges indicate an increased uncertainty up to 10%. Therefore, a maximum measurement uncertainty of $\pm 10\%$ is used as reference for the measured heat fluxes. In addition to the surface temperature measurement, the coaxial thermocouples were also used for heat flux determination using one-dimensional heat conduction and semi-infinite wall assumption. During comparative measurements using coaxial thermocouples and heat flux microsensors with a blackbody source, the heat flux evaluated from the coaxial thermocouples showed only minor deviations from the heat flux microsensor, as long as one-dimensional heat conduction and semi-infinite wall assumption were valid. Therefore, the accuracy of the heat flux determination is also stated as ± 5 to $\pm 10\%$ according to the accuracy of the heat flux microsensor.

IV. Flight Data

A. Flight Trajectory

As shown in Fig. 17, the first rocket stage accelerated the vehicle to a speed of about 768 m/s. After burnout of the first motor and its separation, a short phase without thrust in an altitude range between 2.5 and 8.3 km followed. After a flight time of 14.4 s, the second-stage motor was ignited and provided thrust for about 25 s. The 5 s boost phase of the second stage can clearly be seen in the velocity curve followed by the sustainer phase of approximately 20 s ending at about 39 s. In the ascent phase, the vehicle reached a maximum velocity of 1654 m/s at an altitude of 39 km. After reaching an apogee of 183 km, the descent flight was carried out only aerodynamically without any prior vehicle orientation because no reaction control system was available. The second-stage motor remained attached to the payload during reentry to take advantage of the second-stage fins. The reentry configuration is shown in Fig. 2. Although the initial vehicle attitude before reentry was undefined, the

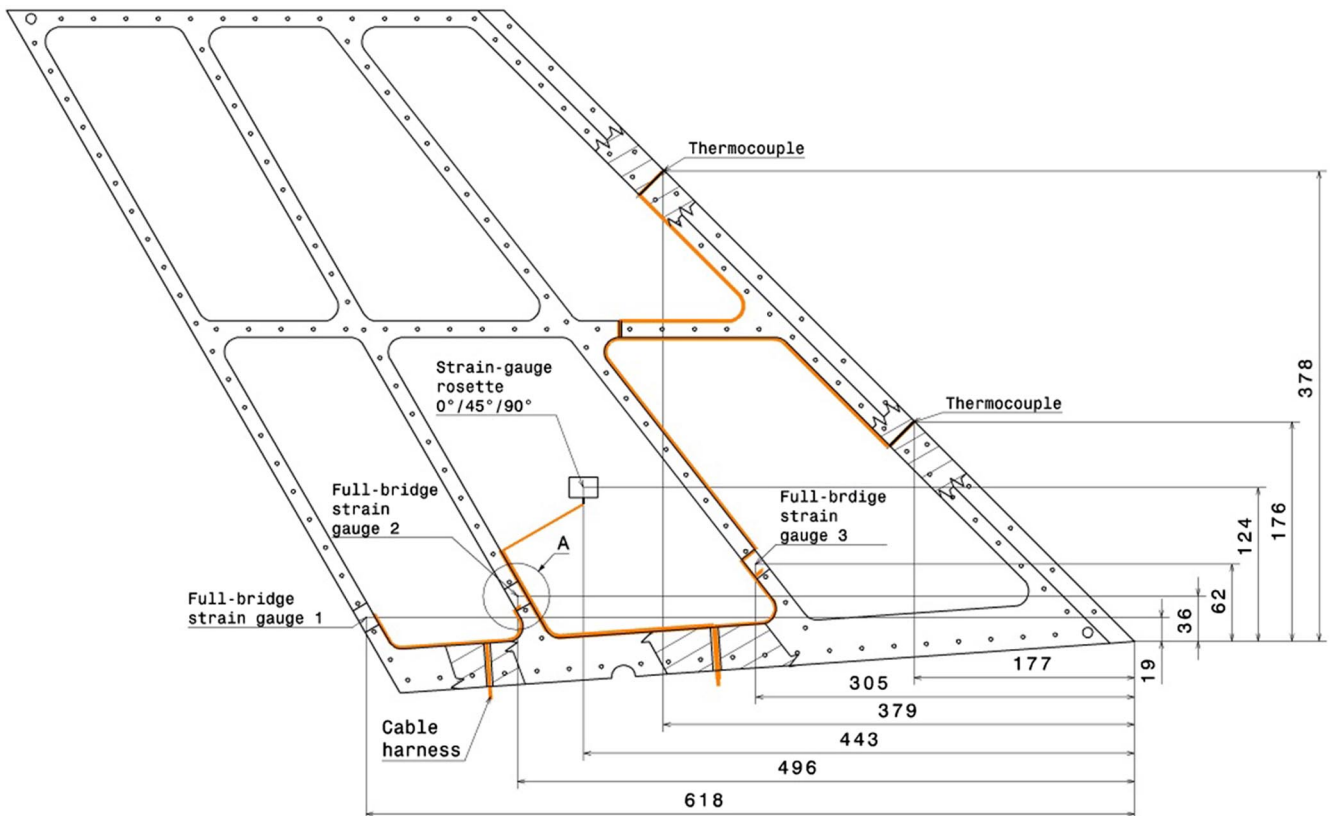


Fig. 15 ROTEX-T fin instrumentation layout.

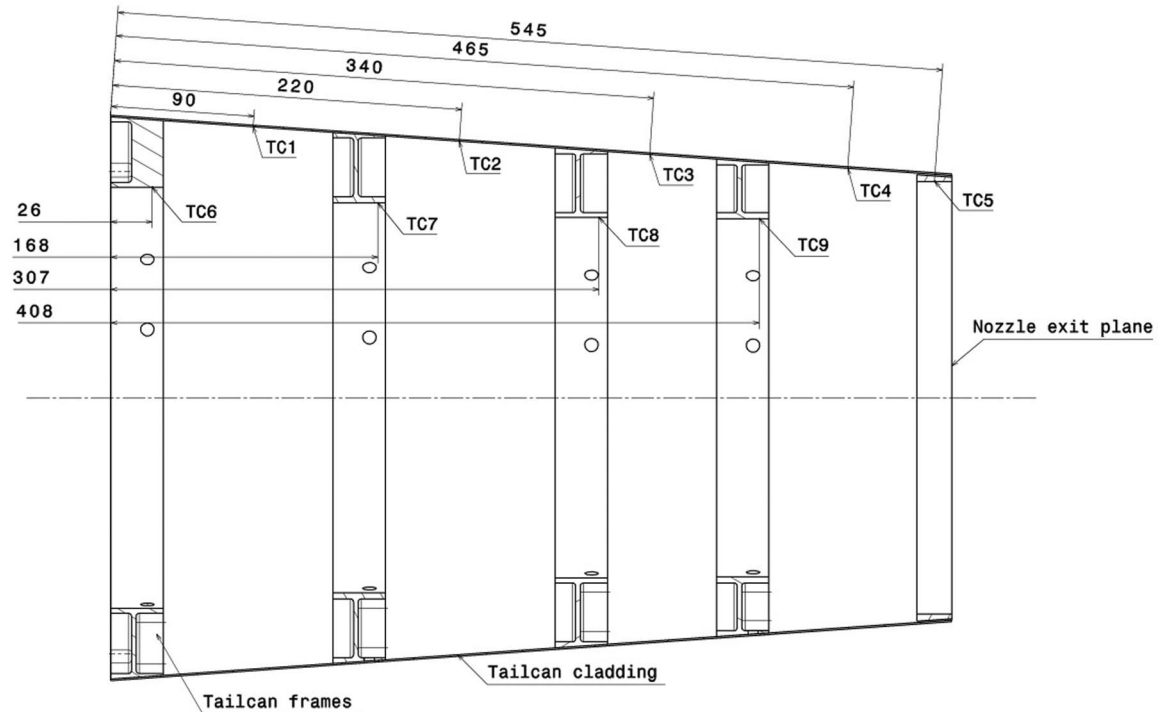


Fig. 16 ROTEX-T tailcan thermocouple instrumentation layout.

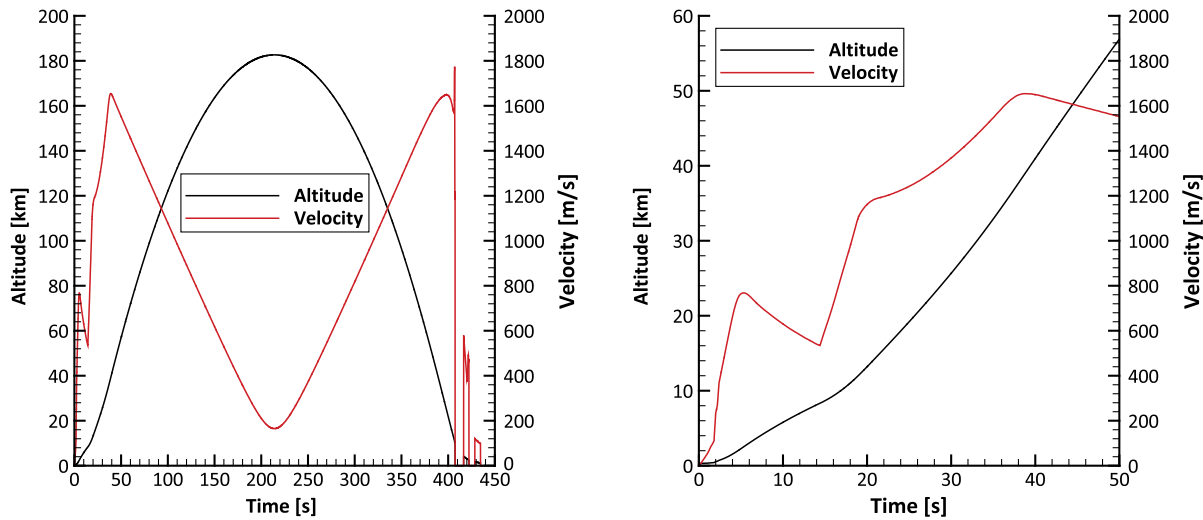


Fig. 17 Flight altitude and velocity of ROTEX-T flight experiment.

four fins of the second stage together with the vehicle's center of gravity location resulted in a self-orientation of the vehicle toward the end of reentry due to increasing atmospheric density.

After reentry, the payload separated from the second-stage motor at an altitude of about 13 km ($t = 405.5$ s) and was afterward decelerated by tumbling. It finally impacted in an uninhabited part of northern Sweden with a speed below 98 m/s, which was the last recorded velocity value before the loss of telemetry. The memory units of the data acquisition systems were designed for a high-impact velocity of the payload and survived the hard landing. After separation from the second-stage motor, the payload telemetry system was still working, and sensor data were received down to an altitude of 1.2 km. Because of the strong tumbling motion directly after separation, some GPS-signal losses occurred, which are visible in the velocity plot in Fig. 17 and were caused by limited GPS satellite visibility.

On the left diagram of Fig. 18, a detailed view of flight Mach and Reynolds numbers is shown during ascent. The necessary

atmospheric parameters (pressure, density, and temperature) were evaluated using data from balloon measurements and the Committee on Space Research International Reference Atmosphere (CIRA)-86 model. Several balloons were launched before the actual rocket launch to check the wind conditions. In addition, one balloon was launched after takeoff of the flight experiment. This balloon was equipped with a pressure and temperature sensor and measured static pressure and temperature up to an altitude of 37 km at which it reached its final altitude. For altitudes above 37 km, the CIRA-86 atmosphere model was used to determine static pressure and temperature. This is visible in the Mach number plots in Fig. 18 at 37 km altitude, at which the determination of static pressure and temperature is switched between balloon measurements and the atmosphere model. Because the static temperature of the atmosphere model does not exactly fit the balloon measurement, a small step is visible in the Mach number curves. The temperature difference at 37 km altitude was about 10 K, leading to a Mach number difference of 0.11 (2.1%).

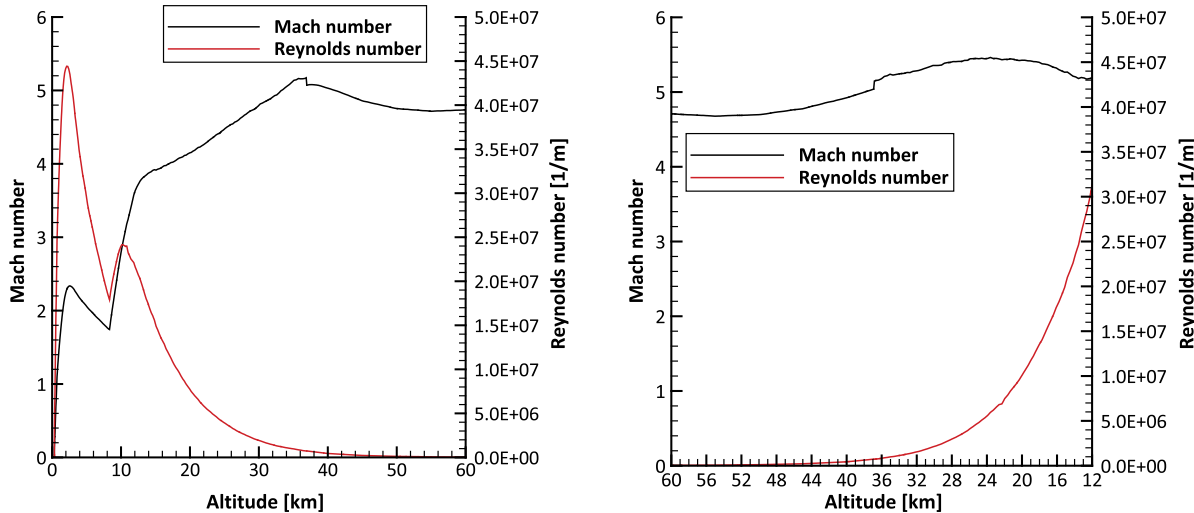


Fig. 18 ROTEX-T Mach and Reynolds number during ascent (left) and descent (right).

During the ascent phase between 0 and 60 km, a maximum Mach number of about 5.1 was reached, corresponding to a velocity of 1654 m/s. The maximum unit Reynolds number of 4.4×10^7 1/m occurred after the boost phase of the first-stage motor at an altitude of 2.2 km. A second peak in the unit Reynolds number with a value of 2.4×10^7 1/m occurred a short time after the ignition of the second-stage motor with a corresponding Mach number of 2.9.

The right diagram of Fig. 18 shows the same curves for the descent phase with a maximum Mach number of 5.46 at an altitude of 23.6 km. Before separation at an altitude of 13 km, the unit Reynolds number increased to approximately 2.7×10^7 1/m.

The uncertainties for the calculated Mach and Reynolds numbers up to 37 km altitude can be determined using the measurement uncertainties for the pressure and temperature sensors on the balloon. Furthermore, the measurement uncertainty of the velocity is needed. The balloon was equipped with a radiosonde including temperature, pressure, and humidity sensors. The data sheet states an uncertainty of ± 0.5 K for the temperature measurement, ± 100 Pa for pressure measurements between 10 and 108 kPa, and ± 60 Pa for pressures between 300 Pa and 10 kPa. The position and velocity of the ROTEX-T vehicle were determined using a Phoenix GPS receiver [8], which was developed by DLR. According to a statement of the developer, the uncertainty of the velocity determination is ± 1 m/s for flight phases with constant acceleration. However, during flight phases with varying acceleration, e.g., first- or second-stage burn phases, the uncertainty can increase significantly. Unfortunately, the velocity uncertainties during phases with strongly varying acceleration have not been investigated so far. Therefore, an estimation has to be used for the uncertainty during the burn phases of the first- and second-stage motors (up to an altitude of 41 km) and during the last phase of reentry (below an altitude of 46 km) due to strong tumbling and deceleration. For the Mach and Reynolds numbers evaluation, a conservative velocity uncertainty of ± 20 m/s was used during these flight phases. For the remaining altitude range, the uncertainty was set to ± 1 m/s due to negligible accelerations. Because the low velocities at the beginning of ascent and the fixed absolute uncertainty for the velocity would lead to very high deviations for Mach and Reynolds numbers, the subsonic regime (up to an altitude of about 0.7 km) was not considered in the uncertainty determination.

The balloon was launched about 16 min after takeoff and took about 2 h to reach its final altitude of 37 km. The maximum measured balloon drift was about 25 km. The variation of atmospheric properties in this area and time period was not considered in the uncertainty evaluation.

Above 37 km altitude, the CIRA-86 atmosphere model was used to determine the static pressure and temperature. This atmosphere model includes zonally averaged monthly mean values of several atmospheric parameters. The model itself does not include uncertainty estimations

for static pressure and temperature. Uncertainties for the CIRA-86 model were evaluated for the SHEFEX-I flight by comparing the calculated values with measurements performed at the SHEFEX-I launch location in northern Norway [9]. The measurements were performed from May to September 1999 for altitudes between 35 and 95 km. Although the launch location of SHEFEX-I was located about 250 km northwest of the ROTEX-T launch site and the measurements were performed about 17 years ago, they are considered acceptable, as no other measured atmospheric data were available for the ROTEX-T launch site above 37 km altitude. According to [9], maximum deviations of $\pm 6\%$ for pressure and $\pm 7\%$ for temperature were used to calculate uncertainties for Mach and Reynolds numbers for the ROTEX-T flight above 37 km height.

The calculated uncertainties are shown in Fig. 19 for ascent and reentry. The shown uncertainties are maximum values calculated using worst-case combinations of the measurement uncertainties for the pressure, temperature, and velocity.

Above 37 km altitude, at which the CIRA-86 atmosphere model was used, the uncertainties are nearly constant due to the assumed constant relative measurement uncertainties for pressure and temperature and the high vehicle velocity, which minimizes the influence of the velocity uncertainty. The step in Mach and Reynolds numbers at an altitude of 41 km during ascent and 46 km during descent is caused by the change of the used uncertainty for the velocity (± 20 or ± 1 m/s). The small step in the Reynolds number curves at an altitude of 16.5 km originates from the change between the two different pressure measurement uncertainties at a static pressure of 10 kPa.

B. Measured Pressure Distribution and Flight Angle Evaluation

The surface pressure distribution on the cone and flare was measured using absolute pressure transducers (XTE-190, 1.7 bar) of the Kulite Company. As shown in Figs. 9 and 11–13 the pressure ports 2, 10, 12, and 15 were placed on the cone at the same axial distance from the nose tip every 90 deg in the circumferential direction. Pressure ports 8, 11, 13, and 16 were placed on the flare in the same manner. The measured pressures on cone and flare are shown in Fig. 20. A slight pressure increase due to passing the sonic speed is visible in all four pressure curves on the cone at an altitude of 700 m. The change in the pressure gradient at an altitude of 8.3 km indicates the ignition of the second-stage motor. Because of the angle of 20 deg, the measured pressures on the flare are significantly higher (Fig. 20, right). In this diagram, the ignition of the second stage is visible more clearly when the pressure gradient changes from negative to positive at 8.3 km height.

At higher altitudes above 35 km, the pressure sensors on the cone measured negative pressure values as shown in Fig. 21, which was caused by the sensor's temperature dependency. Before integration,

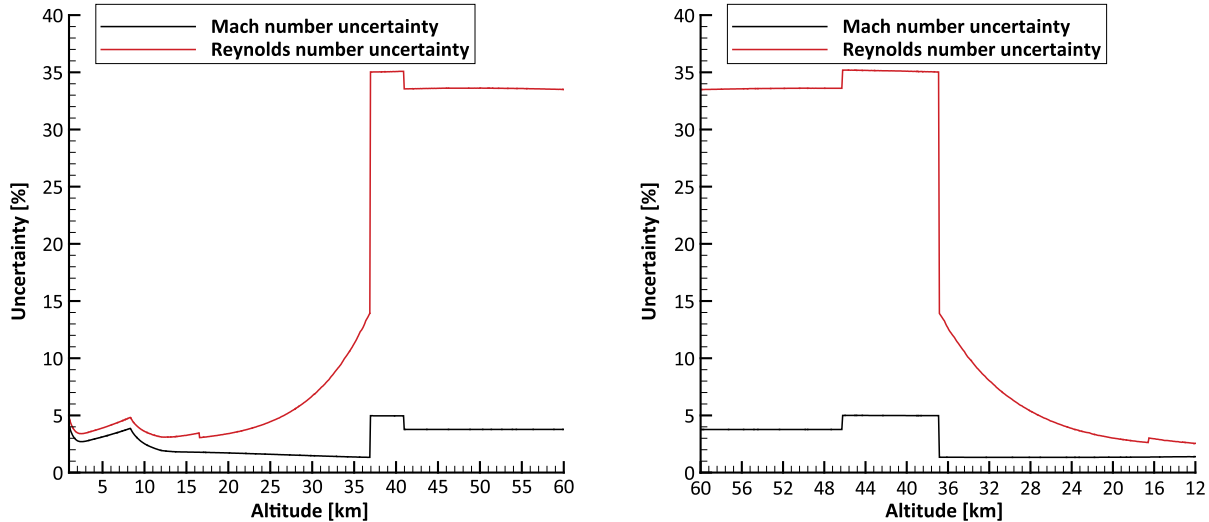


Fig. 19 Uncertainties for flight and atmospheric parameters for ascent (left) and descent (right).

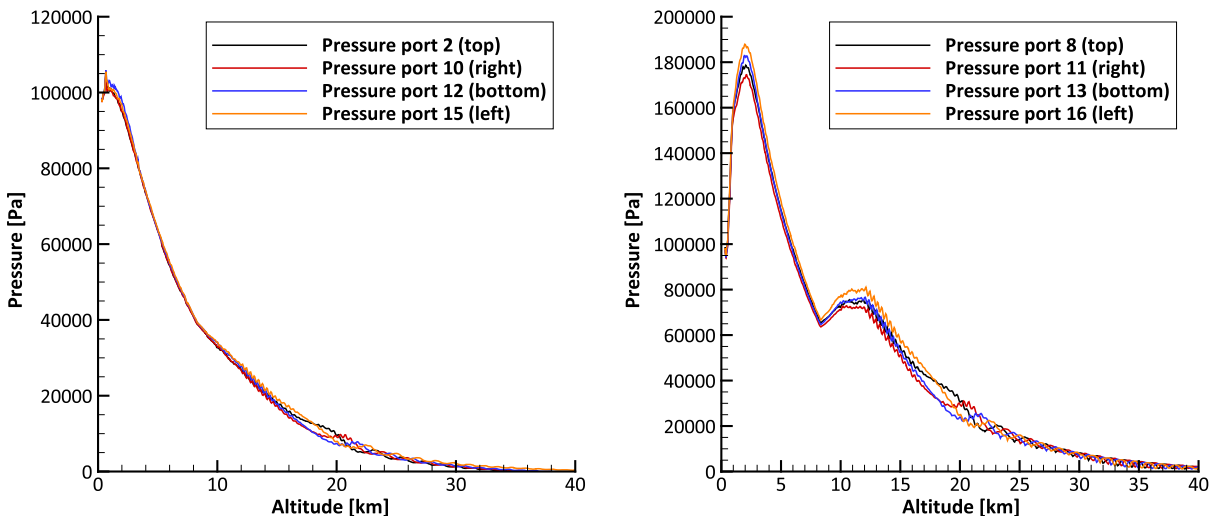


Fig. 20 Measured pressures on cone (left) and flare (right) during ascent.

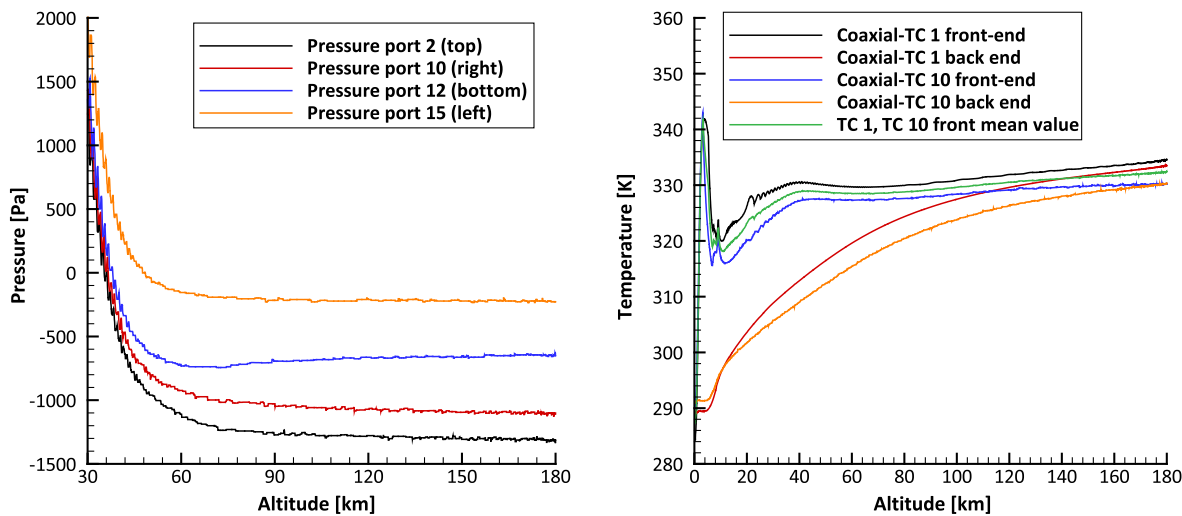


Fig. 21 Pressures on the cone at high altitude (left) and surface temperatures of coaxial thermocouples 1 and 10 (right).

all sensors were calibrated at room temperature in-house at DLR to determine the zero offsets, which are not stated in the data sheets. Although the used sensor type is temperature compensated by design in a large temperature range (298–505 K), it still has a small thermal

zero and thermal sensitivity shift; see Table 2. The performed calibration did not include different temperature levels to determine the exact thermal zero and sensitivity shift, but at least the temperature effects due to thermal zero shift can be compensated

Table 2 Measurement uncertainties for the used sensors

Sensor	Measurement range	Measurement uncertainty	Remark
Pressure sensor (Kulite XTE-190M)	170 and 350 kPa (absolute)	$\pm 0.1\%$ FSO ^a (typical) $\pm 0.5\%$ FSO (max.) Thermal zero shift $\pm 1\% \text{FS}/56 \text{ K}$ ^b (typical) Thermal sensitivity shift $\pm 1\% /56 \text{ K}$ (typical)	Accuracy according to manufacturer data sheet
Type-K thermocouple	198–533 K	Tolerance class 1: $\pm 1.5 \text{ K}$	Polytetrafluoroethylene insulated thermocouple
Type-E coaxial-thermocouple	233–1073 K	Temperature measurement $\pm 1.5 \text{ K}$ (233–648 K) $\pm 0.004 T[\text{C}] $ (648–1073 K) Heat flux ± 5 to $\pm 10\%$	Used for surface temperature measurement and heat flux determination
PCB pressure sensor (model 132A31)	345 kPa	—	Only for dynamic pressure measurement
Heat flux microsensor (HFM 7E/H)	Not specified by manufacturer	± 5 to $\pm 10\%$ ($\pm 5\%$: accuracy specified by manufacturer)	Max. sensor temperature 873 K (short term) 673 K (continuous)

^aFSO means full-scale output.^bFS means full scale.

using the flight data, which is described in the following. A subsequent compensation of the thermal sensitivity shift is not possible because only the overall thermal error at vacuum conditions can be evaluated, which corresponds to the thermal zero shift. But according to the Kulite Company the thermal zero shift is usually the largest component of thermal error, especially when measuring only small fractions of full scale. Therefore, the measurement error caused by thermal sensitivity shift is neglected.

The thermal zero shift is a nonlinear function of temperature, which is different for each individual sensor. If the temperature increase from room temperature is comparably low compared to the overall compensated temperature range, a linear correlation can be assumed for the corresponding temperature interval. Because the pressure transducers were not equipped with temperature sensors, the temperatures of the coaxial thermocouples, which were mounted close by, were used to evaluate the sensor temperature. Therefore, according to Figs. 11 and 13, coaxial thermocouples 1 and 10 were used to determine the pressure sensor temperature. On the right side of Fig. 21, the measured front- and rear-end temperatures of these thermocouples are shown during ascent. Although the temperature-sensitive element of the pressure sensor is also located at the sensor's front end, which is also true for the thermocouples, the temperatures of pressure sensors and thermocouples will not exactly match because of different response times, material properties, sensor layouts, and slightly different locations. To minimize the uncertainty of the temperature estimation of the pressure sensors, the thermal zero shift was evaluated at a height of 180 km at which the front and rear ends of coaxial thermocouples 1 and 10 showed nearly identical temperatures (between 330 and 334 K) and only a very small temporal temperature gradient. This indicates that the surrounding structure, including the pressure sensor, was almost at equilibrium temperature. To evaluate the pressure sensor temperature at 180 km altitude, all four thermocouple temperatures (two front end and two rear end) were averaged, leading to a mean temperature value of 332 K. With a temperature of 291 K during calibration, the maximum pressure sensor temperature increase was only about 41 K during ascent. For the small temperature interval between 291 and 332 K, the assumption of a linear correlation for the thermal zero shift is considered acceptable.

The pressure curves on the left side of Fig. 21 also show constant values for an altitude of 180 km. Using the measured pressures (which are supposed to be 0 Pa for a height of 180 km) and the sensor temperature increase, the thermal zero shifts were calculated for each individual sensor. The resulting values are shown in Table 3.

To evaluate the pressure sensor temperatures during ascent and reentry, the mean value of the front-end temperatures of coaxial thermocouples 1 and 10 was used (green line in Fig. 21, right) to estimate the magnitude of the temperature-dependent zero shift of the pressure sensors. For all the following diagrams, the described temperature compensation was used for the measured pressures on the cone.

Table 3 Calculated thermal zero shift for pressure sensors on the cone

Pressure sensor	Thermal zero shift, Pa/K	Location
2	-32.05	Cone (top)
10	-27.26	Cone (right)
12	-16.01	Cone (bottom)
15	-5.77	Cone (left)

The pressure sensors for the flare were mounted to small aluminum blocks, which in turn were fixed to the interior structure using thermal spacers made from PEEK material. The sensors were connected to the pressure ports at the flare surface via metallic tubing; see Fig. 10. Because of the low thermal conductivity of the PEEK material, the temperatures of these pressure sensors increased weakly during the flight time.

To monitor structural temperatures, several thermocouples were installed on the inner surface of the flare and cone. Two structural thermocouples were mounted near the thermal spacers for the flare pressure sensors. Using these temperature measurements and a numerical thermal analysis, the actual temperatures of the flare pressure sensors were evaluated. The results showed a total temperature increase of 25 K for the complete flight time until the payload separation. For the ascent phase between 0 and 80 km, the calculated temperature increase was only 2 K, and therefore no pressure sensor temperature compensation was necessary. Until the beginning of reentry at 80 km height, the calculated temperature increased to about 310 K, and during reentry until payload separation at an altitude of 13 km, a further temperature increase of 3 K was calculated. Therefore, a pressure sensor temperature compensation was also unnecessary for the reentry phase. To account for the increased sensor temperatures at the beginning of reentry, the pressure sensors on the flare were zeroed at 80 km altitude.

Figure 22 shows the pressures on the cone for an altitude range between 0 and 10 km (left diagram) and 10 and 35 km (right diagram) incorporating the temperature compensation. The altitude axis represents the height above mean sea level (MSL). The Esrange Space Center, where the vehicle was launched, is located at a height of approximately 330 m above MSL, which is therefore the first data point in the diagrams. The green curves in Fig. 22 represent the pressure, which is calculated by solving the Taylor–MacColl equations [10] for the 7 deg half-cone angle and inflow Mach number according to Fig. 18 and assuming a zero angle of attack. Because the Taylor–MacColl equations can only be used at supersonic conditions, the calculation starts at an altitude of 700 m.

In the subsonic flight regime, all sensors show very good agreement. After passing the sonic speed up to an altitude of about 10 km, pressure sensors 2, 10, and 15 measured the same pressure within the measurement uncertainty of the pressure sensors. Only pressure sensor 12 gave slightly higher values than the other sensors for altitudes below 3 km, which indicates a small angle of attack.

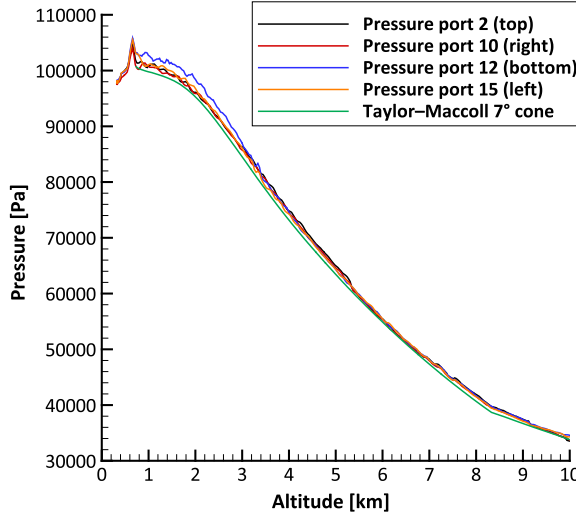


Fig. 22 Detailed view of measured pressures on cone during ascent of ROTEX-T.

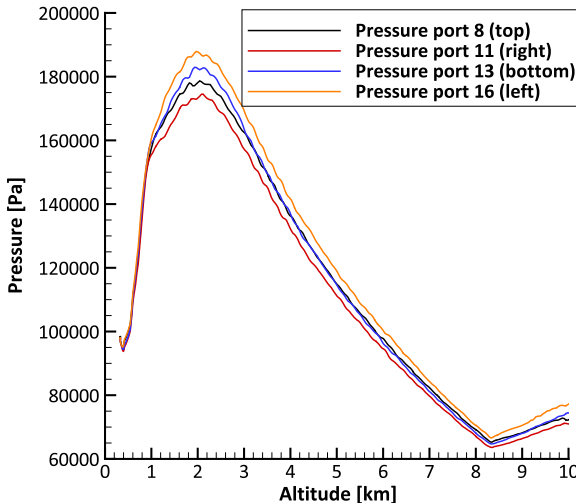
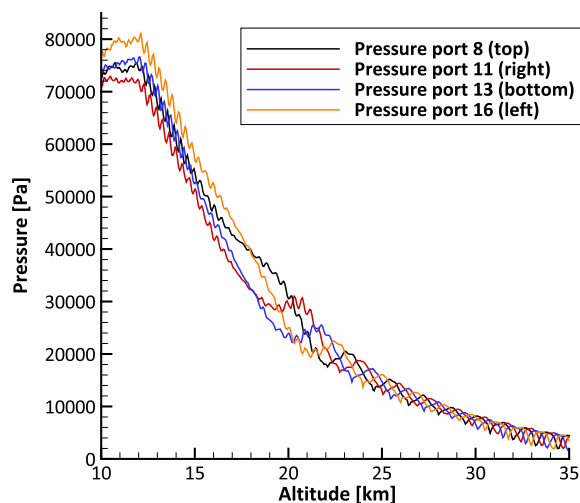
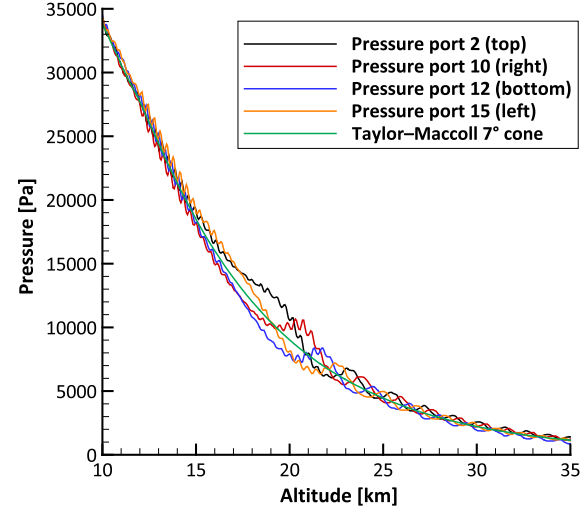


Fig. 23 Detailed view of measured pressures on flare during ascent of ROTEX-T.

But with a nonzero angle of attack, the Taylor–Maccoll curve should be more or less in the middle of the measured pressures as shown on the right side of Fig. 22. Therefore, the deviation of pressure sensor 12 was probably caused by a higher measurement uncertainty compared to the other sensors. Applying the maximum uncertainty of 0.5% (full scale) according to Table 2 would lead to pressure values comparable to sensors 2, 10, and 15. Above 10 km height, the pressure differences started to increase, which is shown in the right diagram of Fig. 22, indicating small flow angles. The pressure oscillations due to spin stabilization can also be seen in this diagram on all four pressure curves.

For flight phases with a low angle of attack/sideslip (small pressure differences), the agreement between the measured pressures and the calculated values using the Taylor–Maccoll equations is good. For the altitude range between 0.7 and 10 km, the deviation is below 3.6%. The variation of the Taylor–Maccoll solution concerning its input parameters (M_∞ and p_∞) can be determined using the corresponding uncertainties for the freestream Mach number and static pressure. For the altitude range up to 10 km, the maximum variation for the Taylor–Maccoll calculation is $\pm 1.4\%$ of the calculated pressure value using an average Mach number uncertainty of $\pm 3\%$ according to Fig. 19 and a static pressure uncertainty of ± 100 Pa for the balloon measurement as described earlier.

For increasing angle of attack and sideslip, the deviation between the measurement and computed Taylor–Maccoll values became larger due to the violation of the zero angle-of-attack assumption, which is visible in the right diagram of Fig. 22.



The measured pressures on the flare, which were higher due to the larger deflection angle, are shown in Fig. 23. For higher altitudes above approximately 12 km shown on the right side of Fig. 23, the pressures were consistent with the pressures measured on the cone. For lower altitudes, shown on the left side of Fig. 23, the measured flare pressures showed different behavior. Above 1 km altitude, the flare pressures indicated a persistent angle of sideslip, which was not measured by the cone pressure sensors and cannot be explained by the sensor measurement uncertainty, even if a higher uncertainty of $\pm 0.5\%$ is used. Flow phenomena like imperfect flow separation and reattachment due to small flow angles, below the uncertainty of the flow angle determination presented in Fig. 29, may have had an influence on the flare pressure distribution. Therefore, further investigations like numerical simulations are necessary to identify possible reasons for the different behavior on the cone and flare.

The measured pressures on the cone and flare during the last phase of descent are shown in Fig. 24. As mentioned before, ROTEX-T was not equipped with a reaction control system, and therefore no attitude control was carried out before or during reentry. The vehicle attitude and trajectory during reentry were only defined by aerodynamic inertia and gravitational forces. The pressures on the cone and flare showed the same behavior with large pressure fluctuations between 35 and 20 km caused by a large oscillating motion of the vehicle combined with vehicle rotation due to increasing spin. Toward the end of the descent phase, the pressure fluctuations got smaller because the oscillation was damped by the second-stage fins, which

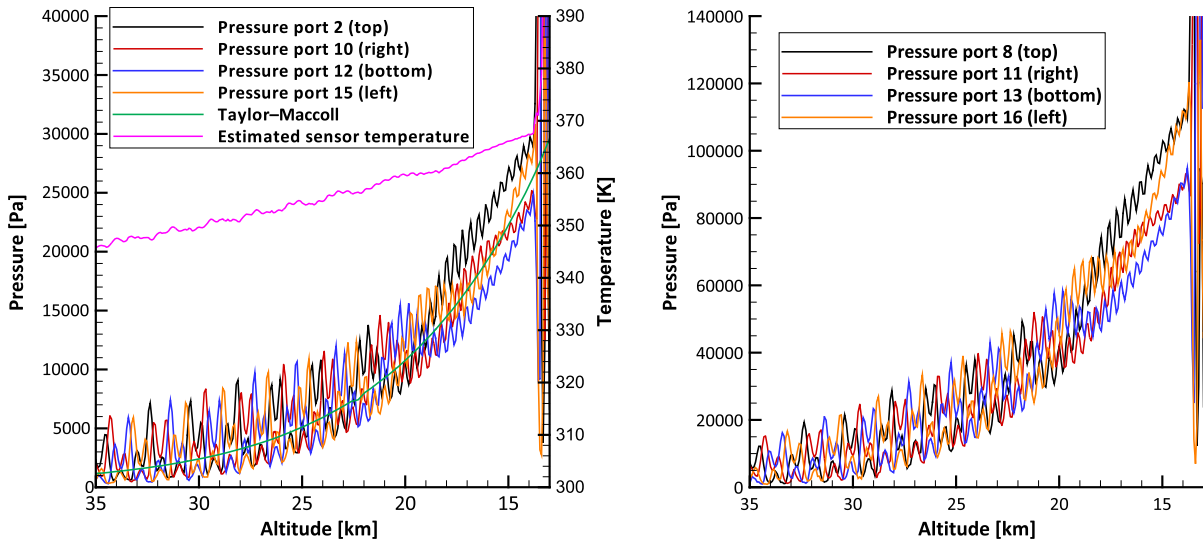


Fig. 24 Measured pressures on cone (left) and flare (right) during last phase of ROTEX-T descent.

got more efficient due to increasing atmospheric density. Directly before payload separation at about 13 km height, the pressures indicated only a small remaining angle of attack and sideslip. At payload separation, all pressure signals showed a sudden strong increase, which was caused by the tumbling motion after separation. On the left diagram of Fig. 24, which shows the measured pressures on the cone, the evaluated pressure sensor temperature and the calculated pressure for zero angle of attack using Taylor–Maccoll are shown in addition.

ROTEX-T was not equipped with an inertial measurement unit, and the flow angles can therefore only be evaluated using the measured pressure values. To determine the flow angles without using complex CFD calculations or wind-tunnel testing, the modified Newtonian law was used to calculate angle of attack and sideslip. In addition to the Newtonian calculation, an approach using the Taylor–Maccoll equations was applied. Both methods are described in the following.

The used coordinate system is shown in Fig. 25 with the x axis pointing in the flight direction, the y axis pointing toward pressure port 15 (left), and the z axis pointing toward pressure port 12 (bottom). The angle of attack and sideslip definitions including the definition of positive rotation are also shown in the figure together with the components of the vehicle velocity vector, u , v , and w .

The modified Newtonian law is given in the following equation with $c_{p,\max}$ calculated using the Rayleigh pitot tube formula ([11] p. 61). With the known Mach number M_∞ , freestream static pressure p_∞ , heat capacity ratio γ , measured static pressure p , cone angle δ , and pressure port clock angle φ , the only two remaining unknowns are the angle of attack α and angle of sideslip β . The clock angle is the clockwise angle looking in the aft direction starting at the top instrumentation line ($\varphi_{PP2} = 0$ deg, $\varphi_{PP10} = 90$ deg, $\varphi_{PP12} = 180$ deg, and $\varphi_{PP15} = 270$ deg>):

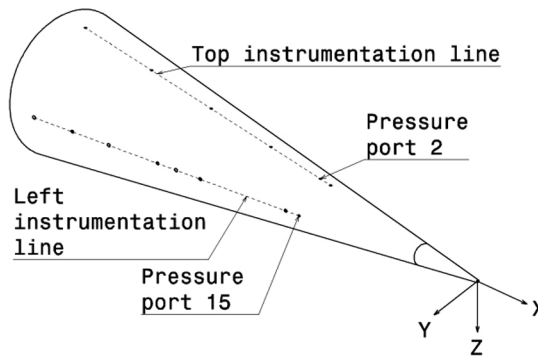


Fig. 25 Coordinate system and angle of attack/sideslip definition.

$$c_p = c_{p,\max} \sin^2 \theta \rightarrow p - p_\infty = \frac{1}{2} c_{p,\max} M_\infty^2 \gamma p_\infty \sin^2 \theta$$

$$\sin \theta = \frac{\mathbf{V}_\infty}{|\mathbf{V}_\infty|} \cdot \mathbf{n} \quad \frac{\mathbf{V}_\infty}{|\mathbf{V}_\infty|} = \begin{pmatrix} \cos \alpha \cos \beta \\ \sin \beta \\ \sin \alpha \cos \beta \end{pmatrix}$$

$$\mathbf{n} = \begin{pmatrix} \sin \delta \\ -\sin \varphi \cos \delta \\ -\cos \varphi \cos \delta \end{pmatrix} \quad c_{p,\max} = f(M_\infty, \gamma)$$
(1)

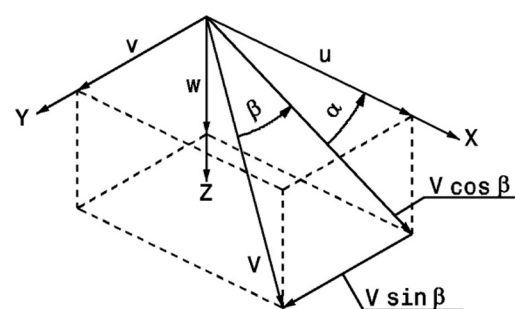
Using the Newtonian law, a separate equation can be written for each pressure port. Combining the two equations for top/bottom and left/right and inserting the corresponding clock angles leads to

$$\frac{p_2 - p_\infty}{p_{12} - p_\infty} = \frac{(\cos \alpha \cos \beta \sin \delta - \sin \alpha \cos \beta \cos \delta)^2}{(\cos \alpha \cos \beta \sin \delta + \sin \alpha \cos \beta \cos \delta)^2}$$

$$\rightarrow \alpha = f(p_2, p_{12}, p_\infty, \delta) \quad (2)$$

$$\frac{p_{15} - p_\infty}{p_{10} - p_\infty} = \frac{(\cos \alpha \cos \beta \sin \delta + \sin \alpha \cos \beta \cos \delta)^2}{(\cos \alpha \cos \beta \sin \delta - \sin \alpha \cos \beta \cos \delta)^2} \rightarrow \beta = f(p_{15}, p_{10}, p_\infty, \delta, \alpha) \quad (3)$$

With Eqs. (2) and (3), the angle of attack and sideslip can be calculated using only the measured pressures on the cone, the cone angle, and the freestream static pressure. The calculated flow angles represent the local angle of attack and sideslip as sensed by the pressure ports. To calculate the freestream values, additional effects have to be considered like bow shock flow deflection or



body-induced upwash and sidewash. This would require additional calibration parameters, e.g., from wind-tunnel measurements. Therefore, these effects are neglected for the presented flow angle calculation.

The second approach to determine the flow angles uses the Taylor–MacColl equations for a cone at zero angle of attack. To incorporate also nonzero angles of attack, the nominal cone angle is increased or decreased by the angle of attack; e.g., with an angle of attack of 2 deg and a cone angle of 7 deg, the lower side of the vehicle is assumed to have a cone angle of 9 deg, whereas the top side would be represented by a cone angle of 5 deg. Because the cone is rotationally symmetric, the same method is also valid for the angle of sideslip. Incorporating a nonzero angle of attack creates an error in the pressure calculation using the Taylor–MacColl equations, e.g., because the crossflow, which induces a pressure gradient laterally around the cone, is neglected. However, for small flow angles, these deviations are considered acceptable for a first evaluation of the angle of attack and sideslip. For the determination of the angle of attack, the Taylor–MacColl equations are solved using the given Mach number and different angles of attack reaching from -5 to $+5$ deg with increments of 0.1 deg, corresponding to cone angles between 2 and 12 deg. The actual angle of attack is then calculated by minimizing the root mean square (rms) value between calculated pressures on the cone leeward and windward sides and measured pressure values of pressure ports 2 and 12 according to Eq. (4). The calculation of the angle of sideslip is identical using the measured pressure values of pressure ports 10 and 15:

$$\text{rms} = \sqrt{\frac{(p_2 - p_{\text{calc,top}})^2 + (p_{12} - p_{\text{calc,bottom}})^2}{2}} \quad (4)$$

In Fig. 26, the calculated angle of attack and sideslip are shown using the Newtonian and the Taylor–MacColl approach. The calculated angles using the Taylor–MacColl approach are slightly larger, but both methods show comparable results. For the complete ascent phase, the flow angles show an oscillating behavior due to nonzero flow angles and spin stabilization of the vehicle. During the first part of ascent between 0 and 15 km, the flow angles are small with an absolute value below 1 deg. Above an altitude of about 12.5 km, the angle of attack starts to decrease with a minimum of -2.7 deg between 19 and 21 km. The angle of sideslip first shows an increase to about 1 deg and then decreases to a value of -3 deg at an altitude of about 21 km. Above 21 km, the angle of attack and sideslip show an oscillating behavior with low frequency and decreasing mean value, which is superimposed on the oscillation due to spin stabilization.

Unfortunately, the reason for the change in flow angles at 12.5 km altitude is unknown. The only flight event that took place at that

altitude was the transition between the boost and sustainer phases of the second-stage motor. This transition may have caused a small disturbance of the flight attitude, and such a disturbance would have been only slightly damped due to the decreasing density at higher flight altitudes.

In Fig. 27, the flow angles are shown for the last phase of reentry between 35 km and payload separation at 13 km altitude. Between 35 and about 25 km, the plots for both angles show several gaps that result from violated boundary conditions for the applied calculation methods. For absolute angles greater than 7 deg, the pressure coefficient on the leeward side is assumed to be zero ($p = p_\infty$) in the Newtonian approach because no expansion is considered. In reality, for higher angles of attack, the pressure on the leeward side can get smaller than the freestream static pressure, leading to a negative value on the left side of Eq. (2). Because the right side of the equation is always positive, no angle of attack can be calculated for this case. The same is true for the angle of sideslip and Eq. (3).

For the Taylor–MacColl method, only flow angles between -5 and $+5$ deg were considered (increments of 0.1 deg) for the current approach. A calculated value of ± 5 deg indicates that no value was found in the valid range between -5 deg and $+5$ deg. Therefore, values of ± 5 deg are blanked for the blue curves in Fig. 27.

Although no actual flow angles could be calculated for some points above 25 km with the described methods, the flow angle curves for descent indicate high values for the angle of attack and sideslip above 25 km caused by a strong oscillating motion of the vehicle due to missing attitude control before and during reentry. As already mentioned in the context of Fig. 24, this motion was damped with increasing density toward the end of reentry due to higher efficiency of the second-stage fins. Directly before payload separation, which is visible in the diagram by the sudden increase in the angle of attack and sideslip around 13 km height, the flow angles decreased to values below ± 2 deg.

As described earlier, the Taylor–MacColl approach determines the flow angles by minimizing the root mean square deviation between measured and calculated pressures incorporating different flow angles using the given Mach number and static pressure. Because the Taylor–MacColl equations are only valid for zero angle of attack and sideslip, an error is introduced by incorporating nonzero flow angles, e.g., due to crossflow effects. Even in the case of zero flow angles, it is still only a numerical approach using different simplifying assumptions like attached oblique shock, negligence of the boundary layer, or ideal gas assumption. To get a first estimation of the accuracy of the calculated flow angles, several CFD simulations were performed with different Mach number and flow angle combinations. The computed pressure coefficients from CFD and the Taylor–MacColl approach were used to get relative maximum pressure deviations for the different cases. The pressure deviations were then incorporated into the flow angle calculation using the Taylor–MacColl approach.

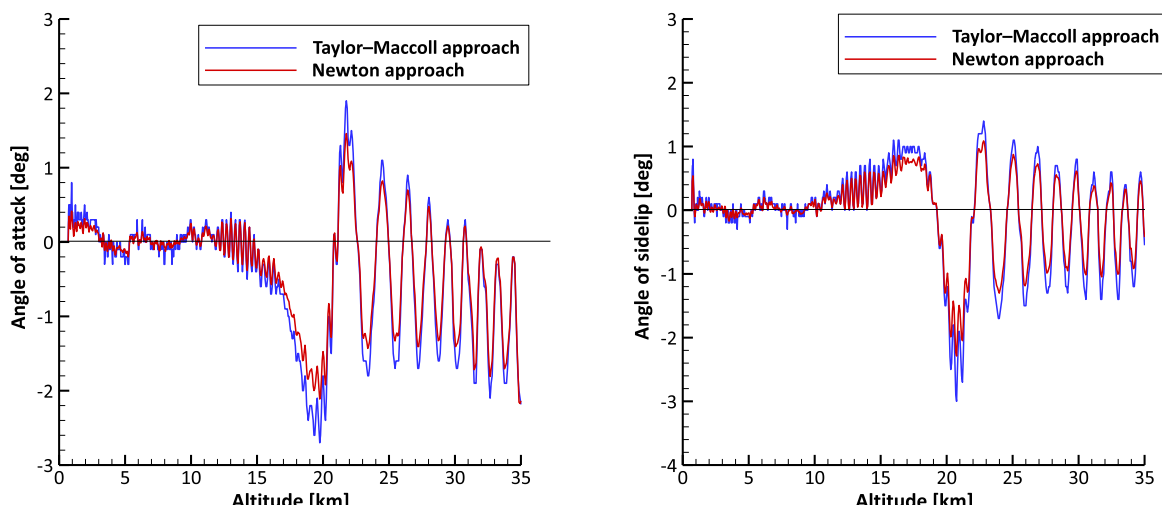


Fig. 26 Calculated angle of attack (left) and angle of sideslip (right) during ascent.

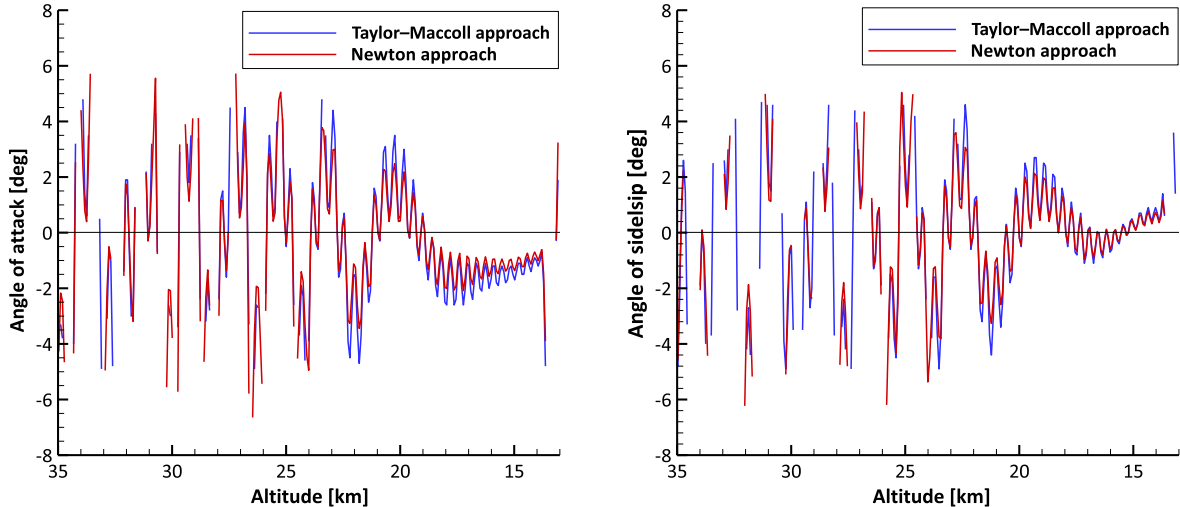


Fig. 27 Calculated angle of attack (left) and angle of sideslip (right) during descent.

Because the flow angles according to the Taylor–MacColl approach and the Newton approach are similar, the flow angle accuracy was only determined for the computed angles according to the Taylor–MacColl approach.

As a first step, only inviscid three-dimensional CFD calculations (Euler) were conducted for the error evaluation using the DLR TAU code [12] to reduce the computation time and mesh generation effort. Although Euler-CFD calculations do not include the boundary layer, they incorporate crossflow effects due to a nonzero angle of attack or sideslip. As a more detailed analysis of the flow angles based on inviscid Euler, viscous laminar/turbulent computations and wind-tunnel data will be presented in a further separate paper, the accuracy of the computed pressure coefficients is considered acceptable for the first error estimation presented in this paper.

The used numerical model included a cone with 600 mm length. The size of the surrounding flowfield was chosen to incorporate also larger flow angles up to 10 deg at various Mach numbers to establish a numerical database for future flow angle determination. It was therefore quite large for the conducted simulations with a low angle of attack and sideslip. A structured grid was used on the cone surface except the nose part and an unstructured grid for the flowfield and nose. The mesh in the nose region is shown on the right side of Fig. 28. To get a fine resolution of the spherical nose, very small elements were used on the nose part. The element length on the cone surface in the x direction was set to a constant value of 1 mm. The circumference at the rear end of the cone was divided into 477 elements corresponding to an element size of 1 mm in the

circumferential direction. Because the circumference at the nose consisted of the same number of elements, the element size in the circumferential direction at the nose part was much smaller. Using these parameters, a very fine resolution on the cone surface was achieved with 2.942×10^5 elements overall. Because grid adaptation increases the computation time significantly when establishing a numerical database with a large number of computations, an overall high resolution of the computational mesh was used so that an accurate result was obtained without the need of grid adaptation. The maximum tetrahedral length scale in the flowfield was set to 6 mm, which resulted in 24.075×10^6 tetrahedral elements for the flowfield. To check the mesh convergence, one simulation case was computed on four different meshes. The results showed that the mesh resolution of the finest mesh shown in Fig. 28 was high enough to get converging pressure coefficients.

On the left side of Fig. 28, the computed pressure coefficient distribution on the cone surface is shown for a freestream Mach number of 4.1 and a value of 3 deg for the angle of attack and sideslip.

Overall, eight representative cases were computed, and the results are summarized in Table 4. The table shows the computed pressure coefficients according to CFD and the Taylor–MacColl approach for the locations of pressure sensors 2, 12, 10, and 15. The right column gives the absolute value of the maximum relative static pressure deviation between CFD and the Taylor–MacColl approach including all four sensors according to the following equation derived from the pressure coefficient definition:

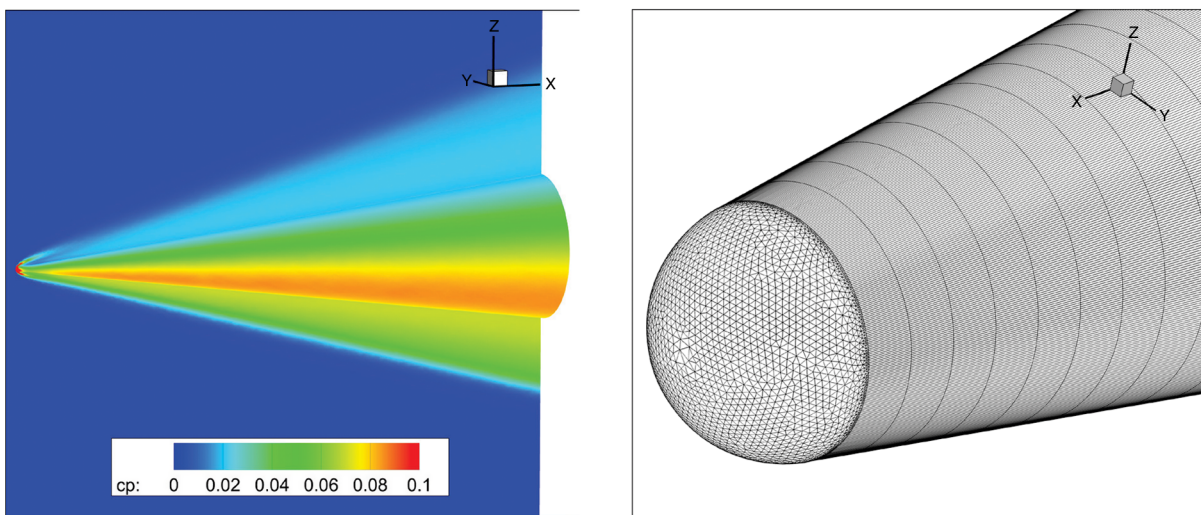


Fig. 28 Calculated pressure coefficients for $M_{\infty} = 4.1$, $\alpha = \beta = 3$ deg (left) and numerical mesh in the nose region (right).

Table 4 Comparison between three-dimensional CFD and Taylor–Maccoll calculations for different flight conditions

No.	M_∞	α	β	Pressure coefficients: three-dimensional CFD				Pressure coefficients: Taylor–Maccoll				Max. static pressure deviation, %
				cp ₂	cp ₁₂	cp ₁₀	cp ₁₅	cp ₂	cp ₁₂	cp ₁₀	cp ₁₅	
1	2	1	1	0.050	0.066	0.050	0.066	0.046	0.073	0.046	0.073	1.56
2	3	1	1	0.041	0.057	0.041	0.057	0.038	0.061	0.038	0.061	1.86
3	4.1	0	0	0.043	0.043	0.043	0.043	0.043	0.043	0.043	0.043	0.02
4	4.1	3	0	0.023	0.071	0.04	0.04	0.017	0.079	0.043	0.043	5.28
5	4.1	3	3	0.019	0.069	0.019	0.069	0.017	0.079	0.017	0.079	6.73
6	5	0	0	0.040	0.040	0.040	0.040	0.040	0.040	0.040	0.040	0.13
7	5	2	0	0.026	0.058	0.039	0.039	0.023	0.062	0.040	0.040	3.70
8	5	2	2	0.025	0.057	0.025	0.057	0.023	0.062	0.023	0.062	4.42

$$\frac{p_{CFD} - p_{TM}}{p_{CFD}} = \frac{(1/2)M_\infty^2\gamma(c_{p,CFD} - c_{p,TM})}{((1/2)M_\infty^2\gamma c_{p,CFD} + 1)} \quad (5)$$

As presented in Table 4, the computed cases with zero angle of attack and sideslip show a very good agreement between the Taylor–Maccoll approach and CFD calculations with pressure deviations below 0.13%. With an increasing angle of attack and sideslip, the deviation increases with a maximum of 6.73% for 3 deg flow angles.

To get representative accuracies for the calculated pressures, the ascent flight was divided into three altitude ranges, and the angle of attack and sideslip were treated separately. Between 0 and 17.8 km altitude, the angle of attack was low between -1.2 and $+0.7$ deg (besides a small peak of 0.8 deg at 0.95 km height) according to Fig. 26. The Mach number in this altitude range varied from 0 to 4. For this altitude range, a pressure deviation of 1.86% according to case 2 was used. Between 17.8 and 20.7 km, the angle of attack decreased to a minimum of -2.7 deg. The Mach numbers for this part of the flight were nearly constant with values between 4 and 4.2. Because in this altitude range the angle of sideslip also decreased to a minimum of -3 deg, case 5 was used with a maximum deviation of 6.73%. Above 20.7 km up to 35 km, the angle of attack oscillated with a maximum of $+1.9$ deg and a minimum of -2.2 deg at Mach numbers between 4.2 and 5.1. The angle of sideslip also oscillated in this altitude region with slightly lower minimum and maximum values. Therefore, the pressure deviation according to the last computed case (4.42%) was applied for the accuracy evaluation. The pressure deviations for the angle of sideslip were evaluated accordingly to 1.86% (0–19.8 km), 6.73% (19.8–21.7 km), and 4.42% (21.7–35 km).

Beside the pressures on the cone, the Mach number and the freestream static pressure were also needed for the flow angle determination. The freestream parameters p_∞ and T_∞ were determined from a balloon measurement, which was launched some minutes after takeoff of the flight experiment. The static temperature was used for Mach number calculation together with the flight velocity measured via GPS. As already described previously, the uncertainty for the static pressure measurement was ± 100 Pa for pressures between 10 and 108 kPa and ± 60 Pa for pressures between 300 Pa and 10 kPa. Because the Mach number uncertainty varied with flight altitude as shown in Fig. 19, three different altitude regimes with different Mach number uncertainties were used according to Fig. 19. An uncertainty of 4% was applied for altitudes below 10 km, 2.5% was applied for altitudes between 10 and 20 km, and 1.7% was applied for altitudes between 20 and 35 km.

The actual estimation of the flow angle accuracy was done using a Monte Carlo analysis because, due to the nature of the calculation approach, the application of linear error propagation was not possible. The determined uncertainties for the input variables presented previously were distributed uniformly, which represents a conservative approach. Overall, 10,000 samples were used for the analysis, and the resulting uncertainties for the flow angle calculation were determined with a 95.4% confidence interval. In Fig. 29, the calculated angle of attack and sideslip are given and include the calculated error bars according to the Monte Carlo analysis. A maximum error of ± 0.9 deg was evaluated for the flow angle determination for altitudes up to 35 km.

The error due to nonzero flow angles depends on the actual angle of attack or sideslip. Since only three cases were considered, and these were evaluated using the maximum flow angles for the corresponding

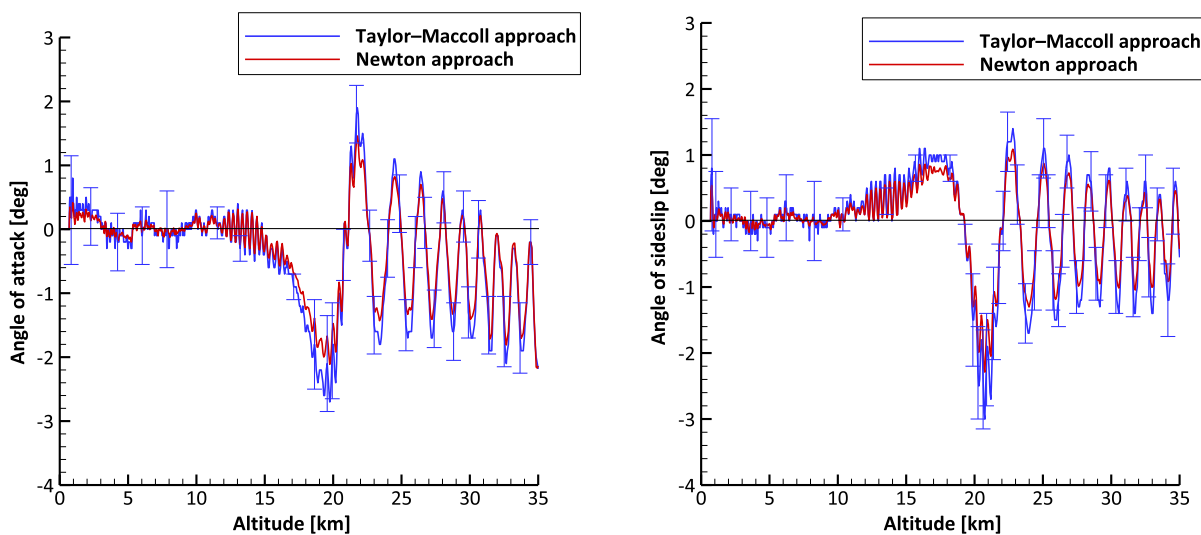


Fig. 29 Calculated angle of attack (left) and angle of sideslip (right) during ascent including error bars.

altitude range, the stated accuracy is conservative, especially for small flow angles at lower altitudes.

C. Measured Heat Flux Distribution

The cone and flare of the ROTEX-T vehicle were equipped with several heat flux microsensors to measure the heat load on the vehicle and the boundary-layer transition during flight. In addition to the microsensors, the temperature measurements of the coaxial thermocouples were used to calculate the corresponding heat flux based on the classical one-dimensional heat conduction model. Because of the high angle of attack and sideslip oscillations during reentry, the heat flux measurements presented in this section are focused on the ascent phase. Figures 30–32 show measured heat fluxes for the sensors 9, 10, and 11, which were located on the left instrumentation line (see Fig. 13).

The diagrams also show the calculated heat flux values using the equations of Korkegi [13,14] and van Driest [14–16] for a laminar and turbulent boundary layer. In addition, the laminar and turbulent heat flux was calculated using the Harris boundary-layer code [17,18]. All three calculation methods are described in the following.

For the incompressible laminar flow over a flat plate, the local skin-friction coefficients can be obtained from classical theory ([11] p. 341). Using the reference temperature method, it is possible to extend the application of these coefficients to compressible flow. In Eq. (6), the local laminar skin-friction coefficient for compressible flow is

given according to Korkegi [13] with a viscosity law modification. The original formula is derived from the reference temperature method using the power law for the temperature dependence of the viscosity. The power law is considered to be slightly less accurate than the Sutherland viscosity law for dilute gases at moderate temperatures. Because the static temperatures during ascent were relatively low, using the Sutherland law should improve the calculation accuracy. Therefore, a modified equation incorporating the Sutherland law instead of the power law was used [14]. To apply the equation for the flat plate to cones, the coefficient can simply be multiplied by the Mangler fraction $\sqrt{3}$ according to ([11] p. 342). The formulas for the corresponding reference temperature and for the running length Reynolds number are also given by Eq. (6).

$$\begin{aligned} c_{f,\text{lam}} &= \frac{0.664}{\sqrt{Re_x}} \sqrt{T^*/T_e} \sqrt{\frac{T_e + 110.4K}{T^* + 110.4K}} \sqrt{3} \\ T^* &= T_e \left(0.42 + 0.58 \frac{T_w}{T_e} + 0.032 M_e^2 \right) \\ Re_x &= \frac{\rho_e u_e x}{\mu_e} \end{aligned} \quad (6)$$

As the Mach number resulting from the Taylor–MacColl equations at zero angle of attack was evaluated directly at the cone surface, it was used as boundary-layer edge Mach number M_e . Because the total temperature T_0 is constant across the bow shock, the temperature T_e at

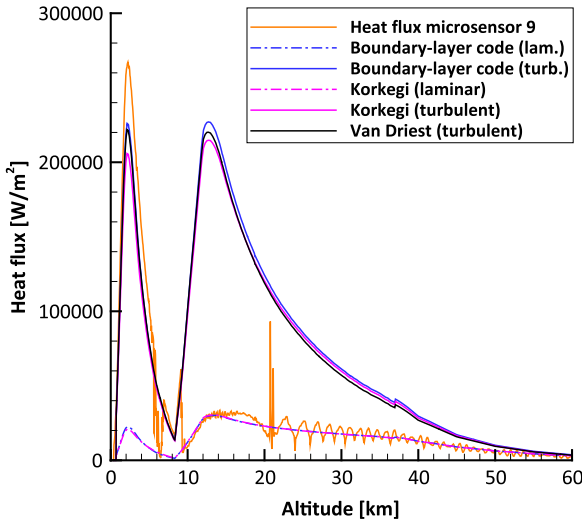


Fig. 30 Measured and calculated heat fluxes for sensor HFM 9 during ascent.

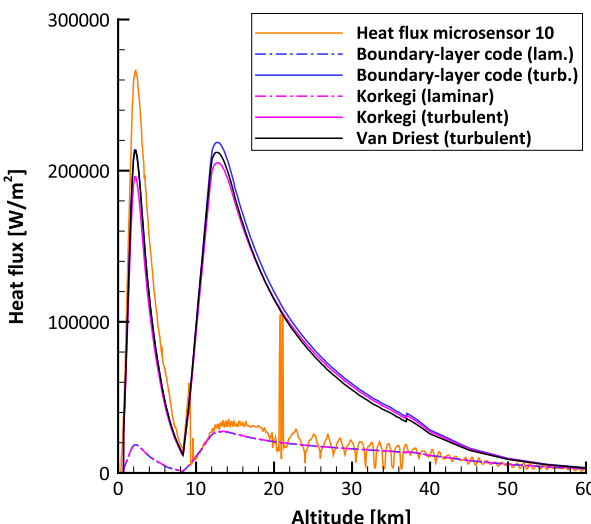
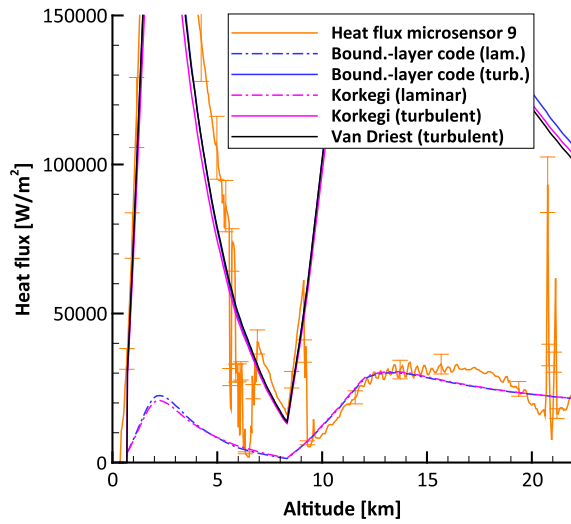
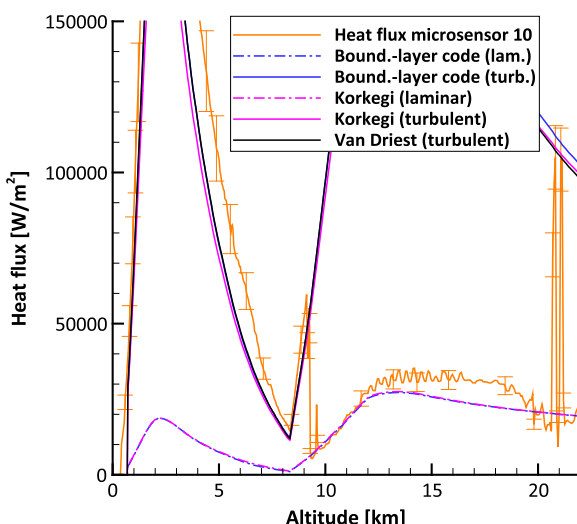


Fig. 31 Measured and calculated heat fluxes for sensor HFM 10 during ascent.



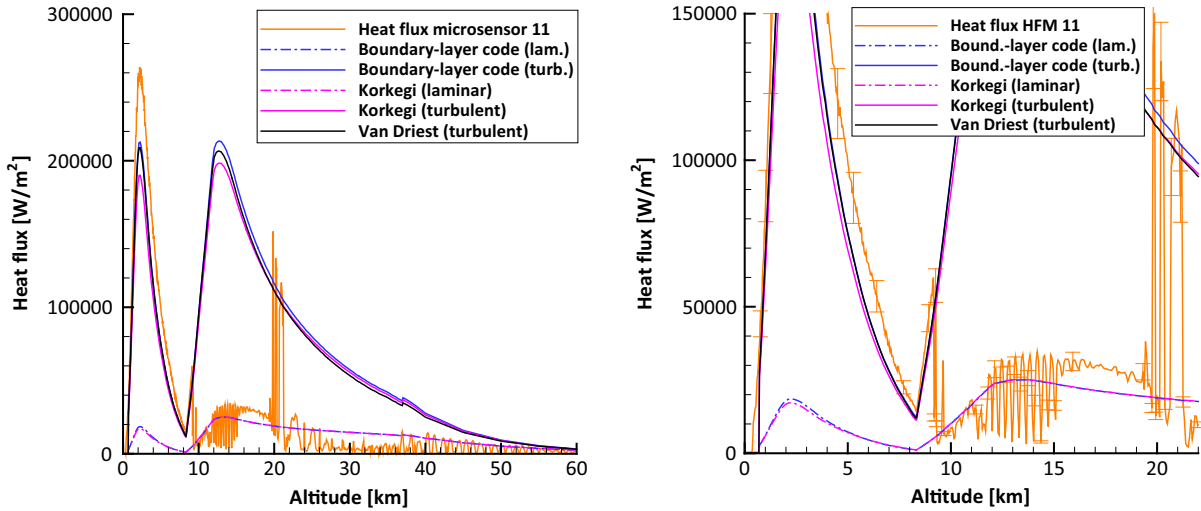


Fig. 32 Measured and calculated heat fluxes for sensor HFM 11 during ascent.

the boundary-layer edge was calculated using the isentropic flow equations and the boundary-layer edge Mach number. The total temperature T_0 was calculated using the flight Mach number M_∞ and the static temperature T_∞ taken from balloon measurement or atmospheric model. If effects like hypersonic interaction and entropy swallowing are neglected, the surface pressure derived by the Taylor-Maccoll equations can be used as the boundary-layer edge pressure on the cone assuming a zero pressure gradient through the boundary layer. With the known edge pressure, temperature, and Mach number, the density ρ_e , velocity u_e , and dynamic viscosity μ_e were evaluated. The parameter x represents the position on the cone surface measured from the virtual apex of the cone.

The local skin-friction coefficient for the turbulent boundary-layer case according to Korkegi [13] and the Sutherland viscosity law modification [14] is given in Eq. (7). To extend the flat plate skin-friction coefficient to cones, the Reynolds number Re_x was divided by 2 [19]. The formula for the reference temperature is also written in Eq. (7) with the additional recovery factor r_{tur} . An empirical relationship, found to be in good agreement with experiments [13], is $r_{\text{tur}} = Pr^{1/3} = 0.9$ using a Prandtl number of 0.71,

$$c_{f,\text{tur}} = \frac{0.0592}{\sqrt[5]{Re_x/2}} \sqrt{\frac{T_e}{T^*}} \sqrt{\frac{T_e + 110.4K}{T^* + 110.4K}} \\ T^* = T_e \left(0.55 + 0.45 \frac{T_w}{T_e} + 0.035 r_{\text{tur}} M_e^2 \right) \quad (7)$$

Using the Reynolds analogy in Eq. (8), the laminar and turbulent skin-friction coefficients were transformed to the corresponding Stanton numbers,

requires laminar and turbulent Prandtl numbers Pr_{lam} and Pr_{tur} . For the laminar Prandtl number, a typical value of $Pr_{\text{lam}} = Pr = 0.71$ was used ([11] p. 292), and for the turbulent Prandtl number, a value of 0.86 was applied [15]. The parameter K is the mixing length proportionality factor for which a value of 0.4 was assumed [15]. Finally, the heat flux was calculated using the Stanton number definition

$$\dot{q}_{w,\text{lam/tur}} = St_{\text{lam/tur}} (\rho_e u_e c (r_{\text{lam/tur}} (T_0 - T_e) + T_e - T_w)) \quad (9)$$

As already stated previously, the turbulent recovery factor was set to $r_{\text{tur}} = Pr^{1/3} = 0.9$. For the laminar case, a recovery factor of $r_{\text{lam}} = \sqrt{Pr} = 0.84$ was used [13]. Because the heat flux microsensors also included a resistance temperature sensing element at the sensor surface, the measured temperatures were used as wall temperatures T_w for the calculation of the heat flux curves shown in Figs. 30–32 according to Eq. (9).

In addition to the local turbulent skin-friction coefficient presented in Eq. (7), a further formula according to van Driest [15] is given in Eq. (10). Because Eq. (10) cannot be solved for c_f directly, the solution was calculated iteratively:

$$\frac{0.242}{\sqrt{c_{f,\text{tur}} F_c}} = 0.41 + \log_{10} \left(\frac{Re_x}{2} F_x c_{f,\text{tur}} F_c \right) \quad (10)$$

As already done for the calculation according to Korkegi, the flat plate skin-friction coefficient was extended for the cone case by dividing the Reynolds number Re_x by 2 [19].

$$St_{\text{lam/tur}} = \frac{Re_{\text{af,lam/tur}} c_{f,\text{lam/tur}}}{2} \quad Re_{\text{af,lam}} = Pr^{-(2/3)} \\ Re_{\text{af,tur}} = \left(Pr_{\text{tur}} \left[1 + 5 \sqrt{\frac{c_f}{2}} \left\{ \frac{1}{5K} (1 - Pr_{\text{tur}}) \left[\frac{\pi^2}{6} + \frac{3}{2} - \frac{3}{2} Pr_{\text{tur}} \right] + Z + \ln \left[1 + \frac{5}{6} Z \right] \right\} \right] \right)^{-1} \\ Z = \left(\frac{Pr_{\text{lam}}}{Pr_{\text{tur}}} - 1 \right) \quad (8)$$

The necessary Reynolds analogy factor Re_{af} is different for laminar and turbulent boundary layers. The corresponding formulas are also given in Eq. (8) for the laminar ([11] p. 326) and turbulent [15] cases. The calculation of the turbulent Reynolds analogy factor

The following transfer functions for compressible flows were used according to Hopkins and Inouye [16] including the additional recovery factor r_{tur} and the Sutherland viscosity law instead of the power law that was originally used by van Driest,

$$F_c = \frac{r_{\text{tur}}((\gamma - 1)/2)M_e^2}{(\sin^{-1}((m - 1 + F)/\sqrt{(m + 1 + F)^2 - 4F}) + \sin^{-1}((m + 1 - F)/\sqrt{(m + 1 + F)^2 - 4F}))^2} \quad F = \frac{T_w}{T_e}$$

$$F_\theta = \frac{\mu_e}{\mu_w} = \left(\frac{T_e}{T_w} \right)^{3/2} \frac{T_w + 110.4K}{T_e + 110.4K} \quad F_x = \frac{F_\theta}{F_c} \quad (11)$$

After c_f was iteratively evaluated, the corresponding heat flux was calculated using Eqs. (8) and (9).

In contrast to the analytical equations for the heat flux calculation presented previously, the Harris boundary-layer code developed by NASA [17] uses an iterative three-point implicit finite element procedure. It solves a laminar, transitional, or turbulent two-dimensional or axisymmetric compressible boundary layer for perfect gas flows. To close the turbulence model, the software includes a two-layer eddy viscosity model. For the given case of a 7 deg cone, the code enables the calculation of the compressible laminar or turbulent boundary layer in a two-dimensional axisymmetric configuration (0 deg angle of attack and sideslip) using cone geometry, inflow conditions, boundary-layer edge conditions, and wall temperature as input parameters. As for the analytical methods, the inflow conditions M_∞ , T_∞ , p_∞ were taken from GPS measurements (flight velocity u_∞) and balloon measurements (p_∞ and T_∞) up to 37 km or the CIRA-86 atmosphere model above 37 km. The boundary-layer edge conditions were again evaluated using the Taylor–MacColl approach at zero flow angle and the isentropic flow equations. Because the code computes the heat flux along the complete cone surface incorporating also the boundary-layer part before the actual sensor position, a wall temperature profile alongside the cone is needed as an input parameter. This profile was generated using all temperature sensors (heat flux microsensors and coaxial thermocouples) on the corresponding instrumentation line. According to Fig. 13, for the left instrumentation line, coaxial thermocouples 10–13 and heat flux microsensors 9–11 were used for the temperature profile. Because no surface temperature measurement was available for the nose tip, the temperature of the structural thermocouple located in the nose tip was used. Temperature values between the individual sensors were interpolated. Neglecting the nose region, the pressure on the cone, calculated by the Taylor–MacColl equations, can be considered constant along the cone surface for zero flow angles.

In Fig. 30, measured and calculated heat fluxes are shown for the position of heat flux microsensor 9 located 671 mm from the nose tip. The maximum measured heat flux value of 267 kW/m^2 was reached at an altitude of 2.2 km approximately at first-stage burnout. At the beginning of ascent, the laminar–turbulent transition took place directly at the nose due to high Reynolds numbers, leading to a completely turbulent boundary layer on the cone surface. With increasing altitude, the laminar region expanded from the nose toward the flare so that a laminar boundary layer would be detected first by sensors at the cone front end. The corresponding calculated heat flux curves for sensor 9 show that the measured heat flux at 2.2 km altitude was at a turbulent level. As expected, the more sophisticated numerical method using the boundary-layer code gives the best agreement with a maximum heat flux value of 226 kW/m^2 , which corresponds to a deviation of -15.4% referred to the measured value. The maximum heat flux values according to Korkegi and van Driest are 206 and 222 kW/m^2 , respectively. Although the absolute deviations of -22.8 and -16.9% are higher, the agreement is reasonable, considering the simplicity of the analytical methods. The small visible step in all calculated curves for turbulent flow at 37 km altitude is caused by the switching between the balloon measurements and atmospheric model for the determination of static pressure and temperature (see also Fig. 18).

On the right side of Fig. 30, the altitude range 0–22 km is enlarged, and error bars of $\pm 10\%$ are included for the heat flux microsensor measurement according to Table 2.

As shown in Fig. 30, the heat flux values decreased after the first-stage burnout caused by decreasing density and velocity. Above an

altitude of 5.5 km, several sudden drops in the measured heat flux down to the calculated laminar values indicate a transitional boundary layer (right side of Fig. 30). For the ascent flight up to 5.5 km, the general agreement between the heat flux measurement and calculated values by the turbulent Harris boundary-layer code is acceptable with deviations between -13.8 and -25.7% referred to the measured value. At 6.9 km height, the transitional behavior ended, and the values increased again to the turbulent level and closely followed the calculated values of the turbulent boundary-layer code up to 9.1 km with deviations between -10 and -21.8% . At an altitude of 9.7 km, the measured heat flux value was again at the laminar level after a transitional behavior between 9.1 and 9.7 km. Up to 13 km height, good agreement is observed between measurements and computed laminar values. The deviation in this altitude range between Korkegi (laminar) and measurement lies between -2 and 40% referred to the measured value. The deviation comparing measurement and the values achieved with the laminar boundary-layer code lies between -3 and 33.8% . Between 10.6 and 13 km, the maximum deviation between the laminar boundary-layer code and measurement reduces to 20.3% .

In the altitude range from 13 to 19.3 km, the deviation between the measured and computed values increases, which was caused by the small positive angle of sideslip shown on the right side of Fig. 26, which violates the calculation assumption of a 0 deg flow angle. The measured heat flux was higher than the calculated one because of the positive sideslip angle (sensor located on the windward side). At 20.7 km altitude, a small heat flux spike is visible in the diagram, which does not completely reach the turbulent level but indicates a short transitional behavior. This was caused by the leeward position of the sensor due to the negative angle of sideslip shown in Fig. 26 at that altitude. It has been observed by many investigators in the past that for a cone the transition on the leeward side moves forward for an increasing angle of attack ([11] p. 331). This was also observed here when, due to the moving transition front, the sensor was again in the transitional region for a short time. Above 21.3 km, the measured heat flux indicates a completely laminar boundary layer, and the measured values in Fig. 30 show an oscillating behavior around the calculated laminar curves due to an oscillating angle of sideslip (Fig. 26). Besides the deviation caused by the nonzero sideslip angle, good agreement between the calculated and measured heat flux is achieved for both theoretical laminar curves.

Figure 31 shows the calculated and measured heat flux for sensor position 10 located 821 mm from the nose tip. Because of its location only 150 mm downstream of sensor 9, the heat flux curves are very similar to Fig. 30. The maximum measured heat flux at 2.2 km altitude was 266 kW/m^2 , and the calculated value according to the turbulent boundary-layer code is 214 kW/m^2 corresponding to a deviation of -19.5% .

According to Fig. 31, the transitional boundary layer at 5.5 km, measured with heat flux microsensor 9, was not detected by heat flux microsensor 10 where the first transition from turbulent to laminar level occurred at 9.1 km, which is identical to the second transition in Fig. 30. With the laminar region expanding from the nose toward the flare with increasing altitude, heat flux microsensor 10 was still located in the turbulent region when heat flux microsensor 9 was already in the laminar region. After transition to the laminar level, the heat flux remained laminar up to an altitude of 20.6 km at which a short transition back to the turbulent level took place, which is identical to the behavior shown by heat flux microsensor 9. In contrast to sensor 9, the transitional behavior lasted longer, and the heat flux completely reached the calculated turbulent level. Above

21.3 km, the measured heat flux showed an oscillation around the calculated laminar values due to the oscillating angle of sideslip as already observed for heat flux microsensor 9. The mean amplitude for heat flux microsensor 10 between 30 and 40 km altitude was larger compared to that of heat flux microsensor 9 with minimum values down to 2.6 kW/m^2 . This was possibly caused by the flare-induced separation bubble extending up to the location of heat flux microsensor 10 in this altitude range due to the larger separation region for a laminar boundary layer. For heat flux microsensor 11 (Fig. 32), the same behavior was observed, but at lower altitudes, because this sensor was located closer to the corner between the cone and flare.

The measured and calculated heat fluxes for heat flux microsensor 11, located at the rear end of the cone 987 mm from the nose tip and about 54 mm from the flare, are shown in Fig. 32. Until transition at an altitude of 9.1 km, the measured and calculated heat fluxes were similar to those of sensor 10 with maximum values of 264 kW/m^2 for heat flux microsensor 11 and 213 kW/m^2 resulting from the turbulent boundary-layer code. After transition above an altitude of 9.7 km, the measured heat flux agrees well with the calculated laminar values up to a height of 11.2 km.

For the altitude range from 11.7 to 15 km, the heat flux oscillated between very small values (down to 3.1 kW/m^2) and values slightly above the laminar level, most probably due to an oscillation of the separation bubble located at the cone–flare junction. The size of the flare-induced separation region varied, and heat flux microsensor 11 was located inside or outside the separation bubble depending on its size, leading to the measured heat flux oscillation. For this altitude range, the heat flux oscillation corresponded well to the measured angle of sideslip oscillation between 0 and 0.8 deg shown in Fig. 26. For a positive angle of sideslip, heat flux microsensor 11 was located on the windward side of the vehicle. On this side, pressure and density were increased, leading to a smaller size of the separation region compared to the zero angle of sideslip case. Because of the smaller separation bubble size, the sensor was located outside the separation region, measuring a slightly higher heat flux than the calculated laminar values caused by the small positive angle of sideslip. At an angle of 0 deg, the sensor was located inside the separation bubble, measuring very low heat fluxes. Between 15 and 19 km altitude, the angle of sideslip was completely positive, and the sensor was located on the windward side of the vehicle outside the separation bubble, leading to a stop of the heat flux oscillation and a measured heat flux above the calculated laminar values. At 19 km height, the angle of sideslip decreased to negative values, and the sensor was located on the leeward side of the vehicle. As already observed for the other two sensors in Figs. 30 and 31, this led to a short transitional behavior with measured heat fluxes reaching the turbulent level. Above 21.3 km, only low heat fluxes were measured with some peaks reaching the calculated laminar level due to the varying angle of sideslip. This indicates that the sensor was mostly located in the separation bubble for altitudes above 21.3 km.

D. Heat Flux Determination Using Coaxial Thermocouple Measurements

The determination of the heat flux from the measured surface temperature is based on the theory of one-dimensional heat conduction into a semi-infinite body with the assumption that during the measurement time the heat penetrating into the sensor does not influence the temperature of the sensor at its rear end. The one-dimensional heat conduction theory yields the following relation between the surface heat flux and the surface temperature signal $T(t)$:

$$\dot{q}_w = \frac{\sqrt{\rho ck}}{\sqrt{\pi}} \left[T(t) + \frac{1}{2} \int_0^t \frac{T(t) - T(\tau)}{(t - \tau)^{3/2}} d\tau \right] \quad (12)$$

For numerical data evaluation, this expression can be transformed to

$$\dot{q}_w = \frac{2\sqrt{\rho ck}}{\sqrt{\pi}} \sum_{i=1}^n \frac{T(t_i) - T(t_{i-1})}{\sqrt{t_n - t_i} + \sqrt{t_n - t_{i-1}}} \quad (13)$$

The determination of the heat flux using Eq. (13) is also known as the Cook–Felderman method [20]. The expression is valid under the assumption that for $t_0 = 0$ the temperature is set to $T(t_0) = 0$, i.e., the temperature in the formula represents the measured temperature difference with respect to the initial temperature, and more important that the sensor rear-end temperature remains constant. The thermal product ρck represents the density, specific heat capacity, and thermal conductivity of the thermocouple material. This value was calibrated individually for each coaxial thermocouple sensor using the contact method (water plunging technique), which, for example, is described in [21]. This method is based on the heat diffusion problem, which arises when two semi-infinite bodies suddenly come into contact, yielding for a certain period of time a constant contact temperature that depends on the two initial temperatures of the two bodies and their ρck values.

Because of the necessary assumption that the sensor rear-end temperature is not influenced by the front-end heat flux (semi-infinite wall), coaxial thermocouples are normally used in short-duration facilities like shock tubes. Although the ROTEX-T flight only lasted about 7.5 min, the semi-infinite wall assumption was only valid for a short time at the beginning of the ascent flight. As presented in Sec. III, the coaxial thermocouple design also included a temperature measurement at the sensor rear end. This measurement was not used in the Cook–Felderman computation due to the assumption of a semi-infinite body. To incorporate the rear-end temperature in the heat flux calculation, a transient one-dimensional thermal finite element simulation (FEM), which is described below in more detail, was set up.

For comparison and validation purposes of the heat fluxes determined by the coaxial thermocouples, several heat flux microsensors and coaxial thermocouples on the flare were mounted side by side with a distance of 18.4 mm for the left and right instrumentation lines as shown in Figs. 11 and 13.

The resulting heat fluxes for heat flux microsensor 7 and coaxial thermocouple 9 on the right instrumentation line are shown on the left side of Fig. 33. For the left instrumentation line, heat flux microsensor 13 and coaxial thermocouple 15 are compared on the right side of Fig. 33. In addition to the Cook–Felderman technique (green curves), the diagrams also show the evaluated heat fluxes according to the transient FEM simulations using the ANSYS tool (blue curves). For these simulations, the coaxial thermocouple was represented by a bar of 18 mm length according to the length of the coaxial thermocouple housing shown in Fig. 14. The bar cross-section consisted of one cell so that the simulation was performed one-dimensionally. In the length direction 400 cells were used with equidistant distribution to accurately determine the temperature penetration into the material and the corresponding surface heat flux. For the density and specific heat capacity of the thermal model, the values of chromel and constantan (type-E coaxial thermocouple) were averaged. The thermal conductivity was evaluated individually for each thermocouple using the thermal product ρck determined during calibration and the averaged density and specific heat capacity. Measured front- and rear-end temperatures of the coaxial thermocouples were applied to model front and rear surfaces, and the simulation was conducted with a fixed time step of 0.05 s for the complete flight time.

As shown on the left side of Fig. 33, the coaxial thermocouple heat flux shows good agreement with the heat flux microsensor measurement for altitudes up to 30 km (33 s after liftoff) with slightly higher deviations during decreasing heat flux levels. The deviation between heat flux microsensor 7 and coaxial thermocouple 9 for the maximum heat fluxes at 2.2 and 12.6 km only amounts to 5 and 1.5%. Above 30 km, the heat fluxes started to differ significantly. Up to 60 km altitude, the heat flux microsensor measurement decreased down to zero, whereas the heat flux determined from the coaxial thermocouple using the Cook–Felderman approach stayed constant. The reasons for this behavior are the violation of the semi-infinite

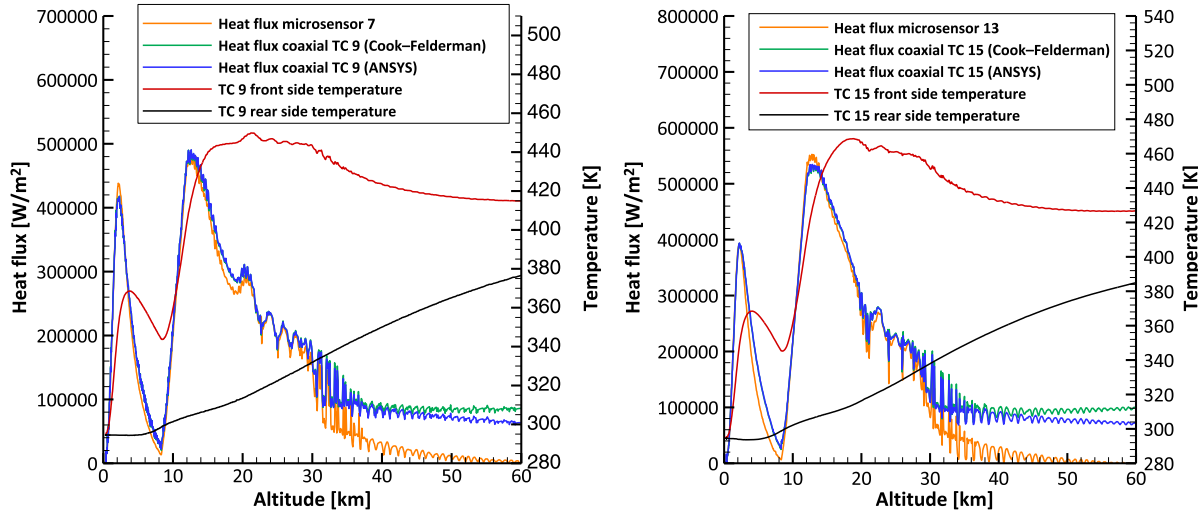


Fig. 33 Heat flux microsensor measurements compared to evaluated heat fluxes using coaxial thermocouples including temperature signals.

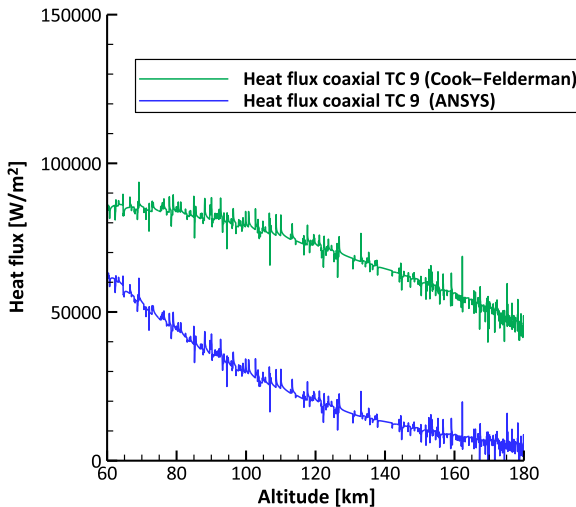


Fig. 34 Evaluated coaxial thermocouple heat flux for TC 9 at high altitudes.

wall assumption and also the thermocouple heating by conduction due to the hot surrounding structure. Front and rear temperatures for coaxial thermocouple 9 are also given on the left side of Fig. 33. The rear temperature of the coaxial thermocouple, measured at the rear end of the thermocouple housing, increased during the complete ascent flight. But as long as the temperature difference between front and rear remained high enough, the Cook–Felderman approach provided accurate heat flux values compared to the commercial heat flux microsensor, although the rear temperature of the coaxial thermocouple was not constant. When the heat flux measured by heat flux microsensor 7 approached zero at around 45 km altitude, the measured front temperature of coaxial thermocouple 9 remained high and only decreased slowly due to conduction. In addition, the difference between the front and rear temperatures got smaller, leading to an increasing error in the Cook–Felderman approach and deviating heat flux values compared to the heat flux microsensor.

The heat fluxes computed using thermal simulations, represented by the blue curves in Fig. 33, give identical results up to 30 km altitude because the influence of the increased rear temperature was low compared to the hot front temperature. With a decreasing difference between the front and rear temperature, the inclusion of the rear temperature takes effect, leading to a slow decreasing heat flux value above 45 km altitude when the heat flux on the cone approached zero as measured by the heat flux microsensor. In Fig. 34, the calculated heat fluxes are presented for altitudes up to apogee. It is clearly visible that the inclusion of the rear temperature in the thermal

simulation (blue curve) leads to a faster decrease of the calculated heat flux compared to the Cook–Felderman approach (green curve).

The heat fluxes on the right diagram of Fig. 33 for heat flux microsensor 13 and coaxial thermocouple 15 also show a good agreement, with slightly higher deviations between the first-stage burnout and second-stage ignition compared to the left diagram. The deviations for the maximum heat fluxes are comparable to coaxial thermocouple 9 with 0.8% deviation at 2.2 km and 3.7% at 12.8 km altitude. Above 30 km altitude, the calculated curves for coaxial thermocouple 15 according to the Cook–Felderman approach and ANSYS show the same behavior as coaxial thermocouple 9.

The left diagram of Fig. 35 shows the measured heat fluxes on the cone for the left instrumentation line up to an altitude of 25 km. In addition, a magnification of the altitude range between 0 and 10 km is presented on the right side of Fig. 35 for better visualization. All coaxial thermocouples except thermocouple 12, which was broken during integration and could not be replaced, are included in the diagram together with the sensor data of heat flux microsensors 9 and 10. The diagram clearly shows the moving transition region during ascent with the laminar boundary layer occurring first at the vehicle front end as indicated by the foremost coaxial thermocouple 10 located 427 mm from the nose tip as shown in Fig. 13. At 5.6 km altitude, the transition region moved in the direction of the flare toward heat flux microsensor 9 and coaxial thermocouple 11, which showed the same behavior as they were mounted relatively close to each other. As heat flux microsensor 10 remained at the turbulent level, the transition was located somewhere between heat flux sensors 9 and 10.

Sensors TC10, TC11, and HFM9 showed an increasing heat flux at 6.5 km altitude due to a transition back to the turbulent level. As the Reynolds number was decreasing between the first-stage burnout (2.3 km altitude) and second-stage ignition (8.3 km altitude), the transition to the turbulent level at 6.5 km height cannot be explained by an increasing Reynolds number. Because this transition occurred in the coasting phase without thrust, an influence like vibration caused by the second-stage motor is also unlikely. A possible cause could be a small negative angle of sideslip, which would have caused the transition to move forward. Although the cone pressures did not indicate an angle of sideslip at that altitude according to Fig. 26, a small angle of sideslip is possible due to the uncertainty of the flow angle determination shown in Fig. 29. Above 8.3 km, the Reynolds number increased due to the increasing flight speed so that the boundary layer remained turbulent. At 9.1 km altitude, all sensors shown in Fig. 35 suddenly dropped to the laminar heat flux level and remained laminar up to 20 km altitude. As the Reynolds number was increasing up to 10 km height, the turbulent–laminar transition was not caused by a decreasing Reynolds number. Because this transition event occurred about 1 s after ignition of the second stage,

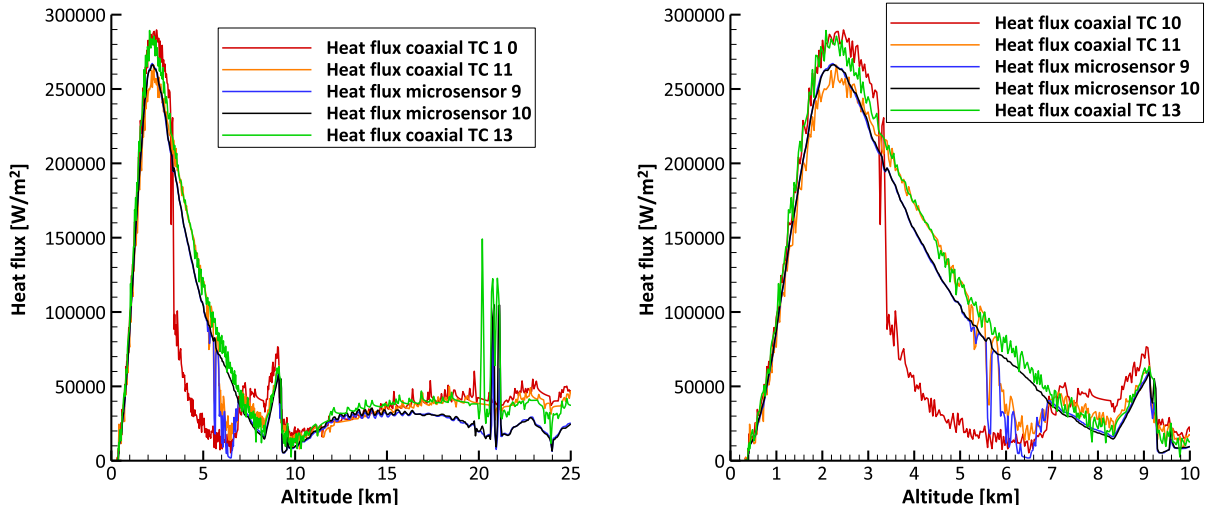


Fig. 35 Heat fluxes for coaxial thermocouples 10, 11, and 13 and heat flux microsensors 9 and 10 between 0 and 25 km altitude.

it is possible that the transition was influenced by the acceleration of the vehicle. In general, a boundary layer is more stable in an accelerated flow, which could even cause a relaminarization of an already turbulent boundary layer. The transition to the laminar heat flux level shortly after the second-stage ignition may therefore have been caused by a relaminarization effect due to the high acceleration in the 5 s boost phase (up to 15 g) of the second-stage motor. But the actual reason for the transition at 9.1 km height requires further investigation. Shortly after the second-stage ignition, the angle of sideslip was increasing as shown in Fig. 26. For a positive angle of sideslip, the left instrumentation line was located on the windward side of the vehicle, which would have caused the transition to move in the direction of the flare. In combination with the decreasing Reynolds number above 10 km altitude, this could explain why the boundary layer remained laminar. At about 20 km altitude, all sensors except coaxial thermocouple 10 showed a short transitional behavior due to a negative angle of sideslip, which caused the transition to move forward to a location somewhere between coaxial thermocouple 10 and 11.

Table 5 summarizes the measured transition events during ascent including the Mach number and Reynolds number for the corresponding sensor positions.

Figures 33 and 35 show that the heat fluxes evaluated using the coaxial thermocouples were suitable for the detection of boundary-layer transition and also show a good agreement with standard heat flux microsensor measurements up to a certain altitude. Although the coaxial thermocouple heat flux evaluation approach is originally only applicable for short-duration measurements, the determined heat

fluxes during ascent indicate that also much longer measurement times are possible depending on the flight conditions.

V. Conclusions

ROTEX-T was successfully launched on 19 July 2016 from the Esrange Space Center near Kiruna in northern Sweden. Although ROTEX-T was carried out as a low-cost flight experiment without an inertial measurement unit, reaction control, and parachute system, several important achievements were made. The launch, boost, stage separation, yo-yo despun, and payload separation were carried out without any anomaly, and a successful payload recovery was achieved. All data acquisition systems worked, and all flight data were recovered successfully from the onboard memory units after impact. Figure 36 shows the payload after impact (left) and all three data acquisition units after payload disassembly (right).

The gathered flight data provided very consistent information, which was analyzed in the postflight analysis presented in this paper. The measured sensor data included heat flux, pressure, and temperature measurements for the complete flight trajectory.

The vehicle reached maximum Mach numbers of 5.1 and 5.46 during ascent and reentry and an apogee of 183 km. Because the vehicle was not equipped with an inertial measurement unit, a numerical approach was used to get a first evaluation of the angle of attack and sideslip during ascent and reentry using pressure measurements of four pressure sensors on the cone. Two different methods were applied for the calculation using the modified Newtonian law and the Taylor–MacColl equations for cones. Besides

Table 5 Measured transition events during ascent for left instrumentation line (stated values indicate the beginning of the transition)

Altitude, km	Transition	Ma_{∞}	$Re_{\infty}, 1/m$	Sensor position along cone, m	Re_{sensor}	Remark
3.4	Turbulent–laminar	2.26	3.86×10^7	0.448 (TC 10)	1.73×10^7	— —
6.7	Laminar–turbulent	1.89	2.3×10^7	0.448 (TC 10)	1.03×10^7	— —
9.1	Turbulent–laminar	2.26	2.15×10^7	0.448 (TC 10)	0.96×10^7	— —
5.2	Turbulent–laminar	2.03	2.84×10^7	0.64 (TC 11)	1.82×10^7	Does not fully reach laminar level
6.6	Laminar–turbulent	1.90	2.32×10^7	0.64 (TC 11)	1.48×10^7	
9.1	Turbulent–laminar	2.26	2.15×10^7	0.64 (TC 11)	1.38×10^7	
5.5	Turbulent–laminar	2.00	2.72×10^7	0.694 (HFM 9)	1.89×10^7	
6.6	Laminar–turbulent	1.90	2.32×10^7	0.694 (HFM 9)	1.61×10^7	
9.1	Turbulent–laminar	2.26	2.15×10^7	0.694 (HFM 9)	1.49×10^7	
20.7	Laminar–turbulent	4.18	7.01×10^6	0.694 (HFM 9)	4.86×10^6	Short transitional behavior due to angle of sideslip
9.1	Turbulent–laminar	2.26	2.15×10^7	0.845 (HFM 10)	1.82×10^7	— —
20.6	Laminar–turbulent	4.18	7.05×10^6	0.845 (HFM 10)	5.96×10^6	Short transitional behavior due to angle of sideslip
9.1	Turbulent–laminar	2.26	2.15×10^7	0.927 (TC 13)	1.99×10^7	— —
20.1	Laminar–turbulent	4.15	7.61×10^6	0.927 (TC 13)	7.05×10^6	Short transitional behavior due to angle of sideslip
9.1	Turbulent–laminar	2.26	2.15×10^7	1.013 (HFM 11)	2.18×10^7	— —
19.7	Laminar–turbulent	4.14	8.04×10^6	1.013 (HFM 11)	8.14×10^6	Short transitional behavior due to angle of sideslip



Fig. 36 ROTEX-T payload and data acquisition systems after recovery.

the four cone pressures, the Mach number and freestream static pressure were additional necessary inputs for the calculation methods that were taken from GPS and balloon measurements. The results of the flow angle calculations showed that the angle of attack and sideslip remained small during the ascent phase. Because of the uncontrolled reentry, the flow angles during descent were mostly too large to be calculated with the simplified methods. But at the end of reentry, the flow angles decreased due to aerodynamic damping, i.e., self-orientation of the vehicle. Because both methods were based on several simplifying assumptions, an error estimation was performed using a Monte Carlo analysis including error bounds for all input parameters to determine accuracies for the calculated flow angles. As both methods showed comparable results, the error estimation was only performed for the Taylor–MacColl approach. To evaluate the accuracy of the pressure determination itself using the Taylor–MacColl equations at nonzero angle of attack, several three-dimensional Euler CFD calculations were performed. By comparing the computed pressures of CFD and the Taylor–MacColl approach, error bounds were estimated for the accuracy of the Taylor–MacColl equations at nonzero angle of attack. For the ascent phase up to 35 km altitude, the calculation of the flow angles gave an uncertainty of ± 0.9 deg with a confidence interval of 95.4%.

In summary, it can be stated that using the measured pressures on the cone for vehicle attitude determination gives reasonable results within the accuracy of the presented methods.

Because of the large oscillating motion of the vehicle during reentry, caused by the lack of a reaction control system, the analyses of the measured heat fluxes were focused on the ascent phase. By analyzing the measured heat flux distribution in conjunction with the evaluated angle of attack and sideslip, several flow phenomena like boundary-layer transition and oscillation of the separation bubble between the cone and flare could be observed. To calculate the laminar and turbulent heat flux levels during ascent, two analytical methods were applied according to Korkegi and van Driest, based on the local skin-friction coefficient, reference temperature method for compressible flows, and Reynolds analogy. In addition to the two analytical methods, a fast numerical method using the Harris boundary-layer code developed by NASA was applied.

A comparison between numerical and measured heat fluxes showed overall good agreement for the turbulent level including the maximum heating at the beginning of ascent. A higher deviation was observed between the measurement and analytical methods for the turbulent level, but the agreement was still reasonable considering the simplicity of these methods. For the laminar level, the analytical and numerical methods showed comparable results, which were also in good agreement with the measured values. To summarize the results of the heat flux comparison, it can be stated that the heat flux at maximum heating can be calculated to within 15.4–19.5% of the measured value.

In addition to heat fluxes measured with the heat flux microsensors, the coaxial thermocouple temperatures were also used to evaluate the corresponding heat fluxes using the Cook–Felderman technique.

A comparison with heat flux microsensor measurements on the flare, where coaxial thermocouples and heat flux microsensors were mounted side by side, showed very good agreement up to 30 km altitude with deviations of 0.8–5% for the measured maximum heat flux levels. Above 30 km altitude, the heat fluxes evaluated from the coaxial thermocouples differed significantly because of the increasing influence of the rear temperature compared to the front temperature. This led to an increasing error in the calculation approach due to the violation of the semi-infinite wall assumption (constant rear temperature). In addition to the Cook–Felderman technique, thermal structural analyses, incorporating also the rear temperature of the coaxial thermocouples, were performed. For altitudes above 45 km, the evaluated heat fluxes showed a faster decrease compared to the Cook–Felderman technique but did not reach a zero heat flux level below 180 km altitude. A possible cause for this was conductive heating of the coaxial thermocouples by the hot surrounding structure.

References

- [1] Gülbhan, A., Siebe, F., Requardt, G., Weihs, H., Laux, T., Longo, J., Eggers, T., Turner, J., Stamminger, A., and Hörschgen, M., “The Sharp Edge Flight Experiment SHEFEX I—A Mission Overview,” *Proceedings of the 5th European Workshop on Thermal Protection Systems and Hot Structures*, Vol. 631, ESA Special Publication, 2006.
- [2] Gülbhan, A., Siebe, F., Thiele, T., Neeb, D., Turner, J., and Ettl, J., “Sharp Edge Flight Experiment-II Instrumentation Challenges and Selected Flight Data,” *Journal of Spacecraft and Rockets*, Vol. 51, No. 1, 2014, pp. 175–186.
doi:10.2514/1.A32572
- [3] Thiele, T., Siebe, F., and Gülbhan, A., “SHEFEX-II Flight Instrumentation and Preparation of Post Flight Analysis,” *Proceedings of 7th International Symposium on Aerothermodynamics for Space Vehicles*, Vol. 692, ESA Special Publication, 2011.
- [4] Thiele, T., Neeb, D., and Gülbhan, A., “Post-Flight Hypersonic Ground Experiments and FADS Flight Data Evaluation for the SHEFEX-II Configuration,” *Proceedings of 8th European Symposium on Aerothermodynamics for Space Vehicles*, ESA, March 2015.
- [5] Lorenz, S., and Bierig, A., “Robustness Analysis Related to the Control Design of the SHEFEX-II Hypersonic Canard Control Experiment,” *AIAA Guidance, Navigation and Control Conference*, AIAA Paper 2013-4857, 2013.
doi:10.2514/6.2013-4857
- [6] Olivier, H., Shock Wave Laboratory RWTH Aachen, Aachen, Germany, <http://www.swl.rwth-aachen.de/en/industry-solutions/thermocouples/> [retrieved 14 June 2018].
- [7] Gülbhan, A., Thiele, T., Siebe, F., Klingenberg, F., and Kronen, R., “Main Achievements of the Rocket Technology Flight Experiment ROTEX-T,” *21st AIAA International Space Planes and Hypersonics Technologies Conference*, AIAA Paper 2017-2208, 2017.
doi:10.2514/6.2017-2208
- [8] Montenbruck, O., Gill, E., and Markgraf, M., “Phoenix-XNS—A Miniature Real-Time Navigation System for LEO Satellites,” *3rd ESA Workshop on Satellite Navigation User Equipment Technologies*, NAVITEC 2006, ESA, Dec. 2006.
- [9] Barth, T., “Aerothermodynamische Untersuchungen Facettierter Raumfahrzeuge unter Wiedereintrittsbedingungen,” Ph.D. Thesis,

- Aerospace Engineering and Geodesy Faculty, Univ. of Stuttgart, Stuttgart, Germany, 2010.
doi:10.18419/opus-3837
- [10] Anderson, J. D., *Modern Compressible Flow with Historical Perspective*, 2nd ed., McGraw-Hill, New York, 1990, pp. 296–301.
- [11] Anderson, J. D., *Hypersonic and High-Temperature Gas Dynamics*, AIAA Education Series, 2nd ed., AIAA, Reston, VA, 2006.
doi:10.2514/4.861956
- [12] Langer, S., Schwöppe, A., and Kroll, N., “The DLR Flow Solver TAU—Status and Recent Algorithmic Developments,” AIAA Paper 2014-0080, Jan. 2014.
doi:10.2514/6.2014-0080
- [13] Korkegi, R. H., “Hypersonic Aerodynamics.” Tech. Rept. VKI-CN 9, von Kármán Inst. for Fluid Dynamics, Rhode-Saint-Genese, Belgium, 1962.
- [14] Willems, S., and Gühan, A., “Experiments on Shock Induced Laminar-Turbulent Transition on a Flat Plate at Mach 6,” *5th European Conference for Aeronautics and Space Sciences*, EUCASS Assoc., Rhode-St-Genese, Belgium, July 2013.
- [15] van Driest, E. R., “The Problem of Aerodynamic Heating,” *Aeronautical Engineering Review*, Vol. 15, No. 10, Oct. 1956, pp. 26–41.
- [16] Hopkins, E. J., and Inouye, M., “An Evaluation of Theories for Predicting Turbulent Skin Friction and Heat Transfer on Flat Plates at Supersonic and Hypersonic Mach Numbers,” *AIAA Journal*, Vol. 9, No. 6, 1971, pp. 993–1003.
doi:10.2514/3.6323
- [17] Harris, J. E., and Blanchard, D. K., “Computer Program for Solving Laminar, Transitional, or Turbulent Compressible Boundary-Layer Equations for Two-Dimensional and Axisymmetric Flow,” NASA TM-83207, Feb. 1982.
- [18] Gühan, A., Neeb, D., Thiele, T., and Siebe, F., “Aero thermal Postflight Analysis of the Sharp Edge Flight Experiment-II,” *Journal of Spacecraft and Rockets*, Vol. 53, No. 1, 2016, pp. 153–177.
doi:10.2514/1.A33275
- [19] van Driest, E. R., “Turbulent Boundary Layer on a Cone in a Supersonic Flow at Zero Angle of Attack,” *Journal of the Aeronautical Sciences*, Vol. 19, No. 1, 1952, pp. 55–57.
doi:10.2514/8.2149
- [20] Cook, W. J., and Felderman, E. J., “Reduction of Data from Thin Film Heat Transfer Gages: A Concise Numerical Technique,” *AIAA Journal*, Vol. 4, No. 3, 1966, pp. 561–562.
doi:10.2514/3.3486
- [21] Jessen, C., “Messung von Druck, Temperatur und Kraft an Modellen im Stoßwellenkanal.” Ph.D. Thesis, Rheinisch Westfälische Technische Hochschule Aachen Univ., Aachen, Germany, 1993.

K. T. Edquist
Associate Editor